Two distinct modes of hemodynamic responses in the human brain

Samira M. Epp[1,2,7], Gabriel Castrillón[1,7], Beija Yuan[3], Jessica Andrews-Hanna[4,5], Christine Preibisch[1,6], Valentin Riedl[1,7]

[1]*Technical University of Munich, School of Medicine and Health, Department of Neuroradiology, Neuroimaging Center, Munich, Germany*
[2]*Ludwig-Maximilians-University, Graduate School of Systemic Neurosciences, Munich, Germany*
[3]*University of California, Department of Bioengineering, San Diego, California, USA*
[4]*University of Arizona, Department of Psychology, Tucson, AZ, USA*
[5]*University of Arizona, Cognitive Science, Tucson, AZ USA*
[6]*Technical University of Munich, School of Medicine and Health, Klinikum rechts der Isar, Clinic for Neurology, Munich, Germany*
[7]*Friedrich-Alexander-University, Department of Neuroradiology, Erlangen, Germany*

ABSTRACT

Functional magnetic resonance imaging (fMRI) detects changes in brain activity by measuring fluctuations in blood oxygenation. While fMRI assumes a fixed relationship between changes in cerebral blood flow (CBF) and metabolic activity, its uniform application across the human cortex lacks complete validation. We used quantitative fMRI together with blood oxygenation level-dependent (BOLD) fMRI to assess oxygen metabolism against both positive and negative BOLD signal changes. We found a surprising mismatch between changes in oxygen consumption and the direction of BOLD signal changes (ΔBOLD) in 14-33% of voxels with significant positive, and in 50-66% of voxels with significant negative ΔBOLD. This implies that a substantial number of voxels with negative ΔBOLD actually demonstrate increased metabolic activity, and vice versa. Contrary to the canonical hemodynamic response model, discordant voxels cover their oxygen demand predominantly via changes in the oxygen extraction fraction (ΔOEF) and not via ΔCBF. This coincides with a higher vascular density and a lower OEF during baseline that we identified in discordant voxels. In summary, we identified a second type of hemodynamic response mechanism for regulating oxygen supply in the human brain. Our results suggest that the classical interpretation of positive and negative BOLD signal changes in terms of increased or decreased neural activity may be too simplistic and we recommend incorporating quantitative MRI or additional CBF measurements for a more accurate assessment of neuronal activity.

INTRODUCTION

fMRI is a powerful method for investigating the neuronal foundations of human perception and cognition (Kim & Ogawa, 2012). The interpretation of its BOLD signal relies on the assumption that CBF changes locally in response to neural activity – assuming fixed neurovascular coupling (Attwell et al., 2010; Drew, 2022; Hall et al., 2016; Hillman, 2014; Howarth et al., 2021; Leithner & Royl, 2014; Phillips et al., 2016). When neurons are active, the cerebral metabolic rate of oxygen (CMRO2) increases. Early studies using positron emission tomography (PET) have demonstrated that a modest increase in CMRO2 is accompanied by a much larger increase in CBF (Fox et al., 1988; Fox & Raichle, 1986), resulting in a ΔCBF/ΔCMRO2 ratio (*n*-ratio) of approximately 2-4 and, consequently, a positive BOLD response (Ances et al., 2008; Buxton, 2010; Uludağ et al., 2004). Although the regulatory mechanisms of this hemodynamic response are still subject to debate (A. D. Ekstrom, 2021; Hillman, 2014), this

overcompensating CBF likely maintains the partial pressure of oxygen in capillaries to allow diffusion into brain tissue (Buxton, 2020, 2023; DiNuzzo et al., 2023).

At the macroscopic level of an fMRI voxel, the BOLD signal is a complex amalgamation of microscopic alterations in CBF, cerebral blood volume (CBV), and OEF, the percentage of oxygen extracted during capillary passage (Buxton, 2010; Buxton & Frank, 1997; Hyder, 2010). Research groups have employed extensive experimental setups to concurrently investigate neuronal activity and hemodynamic changes, revealing a positive correlation between increased neural spiking or synaptic activity and increased CBF or BOLD signals (Boorman et al., 2010; Devor et al., 2003; Gagnon et al., 2015; Logothetis et al., 2001; Siero et al., 2013). By controlling for the extent of sensory input, others have identified a linear relationship between incoming spiking activity and positive ΔBOLD (Heeger et al., 2000; Hyder et al., 2010; Rees et al., 2000; Vanzetta & Grinvald, 1999). Accordingly, colleagues have reported decreased neuronal activity or inhibitory processes related to negative ΔBOLD (Devor et al., 2007; Fracasso et al., 2022, S. 20; Mullinger et al., 2014; Pasley et al., 2007; Shmuel et al., 2002, 2006; Stefanovic et al., 2004; Wilson et al., 2019). Collectively, these studies have enabled us to interpret voxels with BOLD signal changes as localized changes in neuronal activity.

However, numerous studies have also challenged the prevailing notion that BOLD signals are consistently and directly linked to neuronal activity. Notably, experiments involving pharmacological and oxygenation challenges have demonstrated alterations in CBF or CBV without corresponding changes in BOLD signals, thereby suggesting the possibility of a decoupling of the hemodynamic response from neuronal activity under specific conditions (Nagaoka et al., 2006; Rossetti et al., 2021; Zaldivar et al., 2014; Q. Zhang et al., 2019). Other studies reported a lack of change in glucose metabolism associated with ΔBOLD (Devor et al., 2008; Stiernman et al., 2021). In addition, the BOLD signal seems to be modulated by mechanisms other than direct neuronal activity (Boynton, 2011; Cardoso et al., 2012; Das & Sirotin, 2011; A. Ekstrom, 2010; Sirotin & Das, 2009; Tsvetanov et al., 2020). Collectively, these studies suggest that the BOLD signal may not provide a straightforward readout of neuronal activity levels under all circumstances.

Of particular importance, the evidence supporting a direct and linear hemodynamic response primarily originates from investigations of sensory and motor cortices. Nonetheless, these findings have been used as the basis for interpreting ΔBOLD throughout the entire cortex. Critically, several studies reported regional variability of hemodynamic responses, especially between cortical and subcortical regions (Bergel et al., 2020; Devonshire et al., 2012; Roy et al., 2021; Sanganahalli et al., 2016; Schridde et al., 2008; Shaw et al., 2021a; Shih et al., 2011a). Together, these observations raise doubts as to what extent the canonical hemodynamic response can be generalized to the entire cortex.

Given the intricate nature of these phenomena, our study aimed to comprehensively investigate oxygen metabolism in relation to both positive and negative BOLD responses across the human cortex. To accomplish this, we utilized a quantitative fMRI approach to examine the voxel-wise relationship between metabolic activity and changes in the BOLD signal during various task conditions (Bright et al., 2019; Chen et al., 2022; Christen et al., 2012; Kaczmarz, Hyder, et al., 2020; Kufer et al., 2022; Liu et al., 2020; Pike, 2012). In particular, participants performed tasks that were designed to elicit positive or negative BOLD responses and we compared the amplitude and sign of ΔBOLD to ΔCMRO2 within the same voxels.

RESULTS

Participants underwent neuroimaging using either qualitative BOLD fMRI or quantitative fMRI sequences, and we obtained both imaging datasets while participants carried out four distinct experimental conditions within the same session (Figure 1A & 1B). These four conditions enabled us to identify (1) 'task-positive' regions exhibiting an increase in BOLD signal during a calculation task (CALC) compared to a control task (CTRL), as well as (2) 'task-negative' regions that displayed a negative BOLD response during CALC, expected primarily in the default mode network (DMN). Furthermore, we aimed for (3) positive BOLD responses in the DMN by employing an autobiographical memory task (MEM). Alongside the experimentally controlled baseline (CTRL) we also examined the two tasks (CALC, MEM) compared to an uncontrolled resting state baseline (REST).

Quantitative fMRI measures CMRO2 as a metabolic proxy of neuronal activity. CMRO2 is calculated according to the Fick principle incorporating parameter maps for each component of the hemodynamic response (Figure 1C, and Methods). Figure 1C illustrates brain slices of non-thresholded parameter maps averaged across all participants alongside boxplots with the average cortex values of each subject in each condition. Table 1 provides the mean parameter values across all subjects in the CTRL baseline.

Table 1

Whole gray matter parameter values in CTRL condition, mean ± SD across subjects.

R2' [1/s]	CBV [%]	OEF [ratio]	CBF [ml/100g/min]	CMRO2 [µmol/100g/min]
5.3 ± 0.4	4.8 ± 0.2	0.39 ± 0.04	44.5 ± 7.2	127.8 ± 18.4

However, the BOLD signal represents a composite signal of the neurovascular and metabolic response without discerning the influence of individual factors. The hemodynamic response model of the BOLD signal (Figure 1D) assumes an elevation in CBF in response to neuronal activity that supplies a surplus of oxygen to a stimulated region meaning that the oxygen supply exceeds the increased metabolic demands. This is described by the *n*-ratio (ΔCBF/ΔCMRO2), which commonly adopts values of 2-4, ultimately resulting in a positive BOLD response relative to an experimental baseline (ΔBOLD[%]). In this study, we combined BOLD and quantitative fMRI to test the reliability of the conventional hemodynamic response to metabolic changes across regions and conditions, and in comparison to different baseline states.

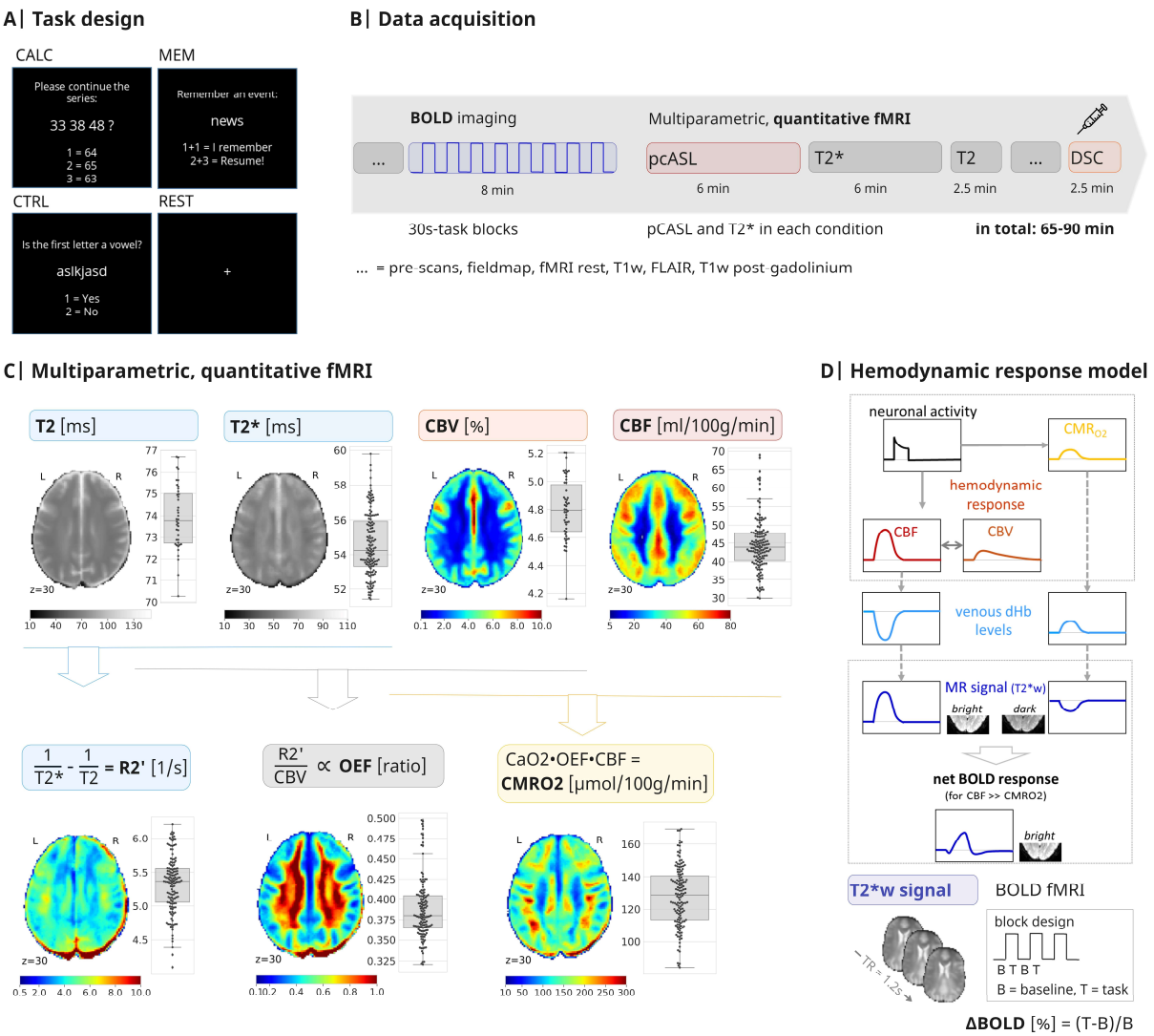

Figure 1. Study design, quantitative fMRI, and the neurovascular coupling model of BOLD fMRI. A| We performed BOLD- and quantitative fMRI on healthy subjects during four different conditions within the same imaging session: calculation task (CALC), autobiographical memory task (MEM), active control baseline (CTRL), and uncontrolled resting-state baseline (REST). **B|** During each imaging session, we acquired BOLD fMRI data with a 30s block design, followed by a block of MR-sequences for quantitative fMRI with conditions in balanced and alternating order: pseudo-continuous arterial spin labeling (pCASL, to measure CBF) and T2* mapping (to measure both reversible and irreversible dephasing) during each condition, and T2 mapping (to measure irreversible dephasing due to tissue properties). At the end of the session, we performed dynamic susceptibility contrast (DSC, to measure CBV) MRI using a contrast agent only during CTRL (to evaluate ΔCBV, we additionally acquired DSC data in a subsample of 10 subjects during CALC). **C|** Quantitative fMRI allows for the quantification of CMRO2 via the integration of T2, T2*, CBV, and CBF. Brain slices of subject-average parameter maps, along with boxplots illustrating average gray matter values per subject and condition (line, median; box limits, upper and lower quartiles). The reversible transverse relaxation rate (R2') reflects the overall deoxyhemoglobin (dHb) content in a voxel. The OEF is proportional to R2'/CBV. Voxel-wise CMRO2 is then calculated as the product of OEF, CBF, and the arterial oxygen content of blood (CaO2). **D|** The hemodynamic response model of the BOLD signal. Increased neuronal activity leads to higher oxygen metabolism (CMRO2), resulting in decreased oxygenation levels and increased dHb content in venous blood. Simultaneously, neurovascular coupling mechanisms cause an increase in CBV and CBF. This hemodynamic response counteracts the effects of oxygen metabolism, leading to a decrease in dHb content. The net fluctuation of dHb levels is dynamically measured with T2*-weighted (T2*w) imaging.

ΔBOLD of any task condition is calculated by subtracting task from baseline T2*w data. Based on this model, positive ΔBOLD [%] is commonly interpreted as increased neuronal activity.

Negative BOLD responses do not necessarily indicate reduced oxygen metabolism

To obtain results that are statistically comparable, we conducted separate analyses using partial least squares (PLS) analyses on BOLD and quantitative (CBF, CMRO2) fMRI parameter maps. These analyses yielded bootstrap ratios (BSR), which are interpreted analogously to z-values (see Methods). The analysis of BOLD data revealed a widespread pattern of significant positive and negative ΔBOLD (Fig. 2A, BOLD). As anticipated, positive ΔBOLD exhibits a greater magnitude than negative ΔBOLD, and the percentage change is higher when the analysis is conducted in native brain space (Fig. 2C, ΔBOLD). At the same time, positive ΔCBF and ΔCMRO2 within the CALC-positive group mask align with a typical hemodynamic response: ΔCBF[%] = 6.7%, ΔBOLD[%] = 0.33%, ΔCMRO2[%] = 2.9%, *n*-ratio = 2.3 (Fig. 2B).

However, the flow and metabolic changes within the CALC-negative mask are less prominent. Overall, ΔCBF and ΔCMRO2 are approximately six times weaker compared to what would be expected for a neurovascular coupling similar to that within positive BOLD regions (ΔCBF[%] = -0.7, *n*-ratio not calculable as ΔCMRO2 is positive). On the subject level, we did not find any significant ΔCBF or ΔCMRO2 (Fig. 2C). In summary, we observe an average increase in metabolism across the entire pattern of positive ΔBOLD, but no significant metabolic changes underlying negative ΔBOLD.

We subsequently employed a region-specific analysis of ΔCMRO2 to investigate whether the absence of metabolic decreases was concealed by the process of averaging across all subjects and voxels in the CALC-negative mask. We identified eight clusters with positive ΔBOLD and nine clusters with negative ΔBOLD distributed across the cortex (Fig. 2D, left). The median ΔCMRO2 is significantly positive in three out of eight BOLD-positive clusters, but negative in none of the BOLD-negative clusters (Fig. 2D, bar plots). The two clusters with negative ΔBOLD in the auditory network (SMN 1, SMN 2) even exhibit a significant positive ΔCMRO2. This indicates that the ΔBOLD-ΔCMRO2 relationship is highly variable at the regional level.

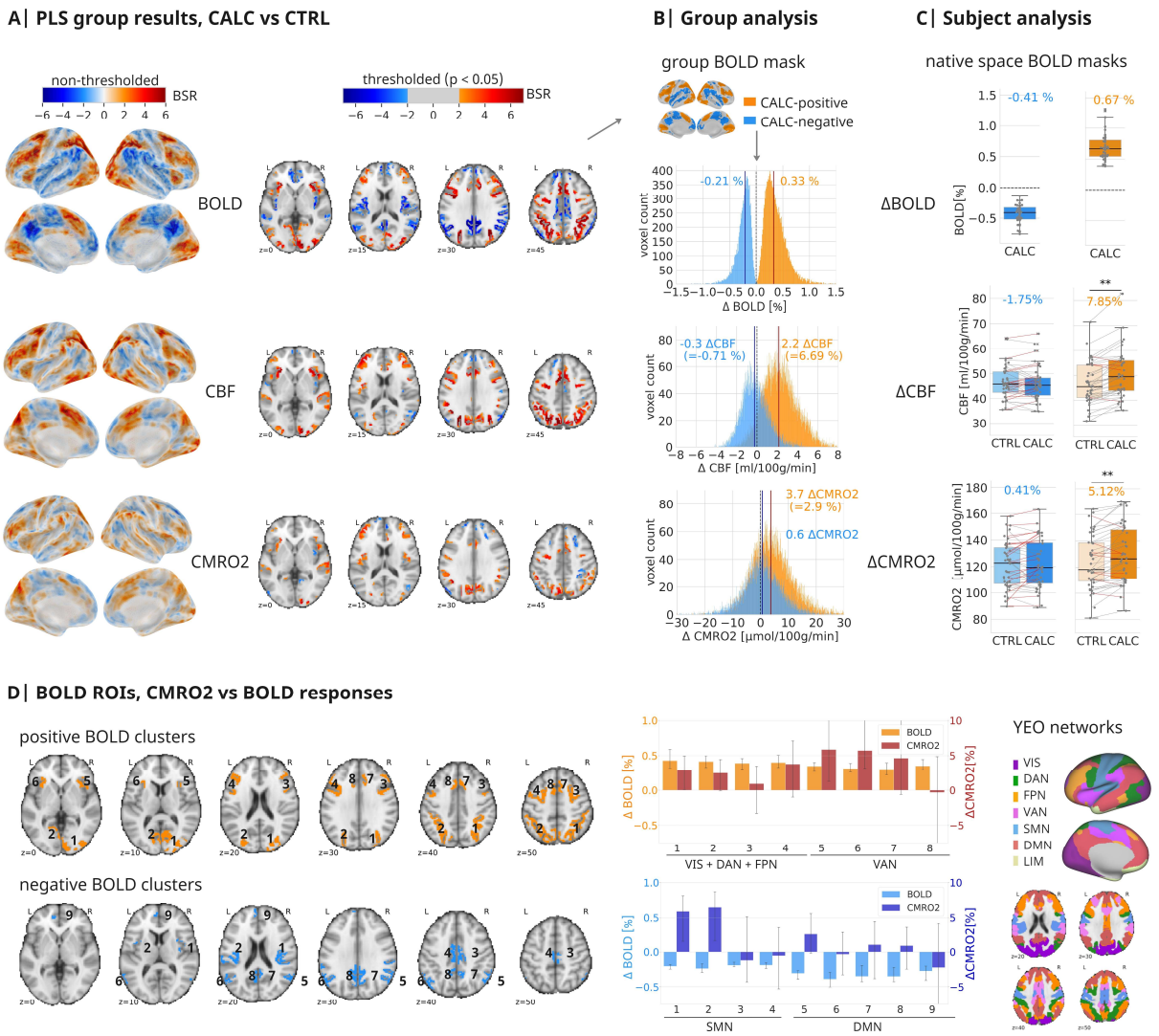

Figure 2. Negative BOLD responses do not necessarily indicate a reduction in oxygen metabolism. A| Statistical results of the PLS group analysis in standard MNI space, comparing CALC and CTRL, for both BOLD and quantitative fMRI parameter maps. Maps projected on the brain surface show non-thresholded bootstrap ratios (BSR, akin to z-values) of the first latent variable, which was significant in each analysis, i.e. for BOLD, CBF, and CMRO2 respectively (permutation tests, $p < .001$). Red voxels indicate higher values during CALC compared to CTRL, while blue voxels represent the opposite contrast. Axial slices display significant brain clusters, thresholded at BSR ±2 (akin to $p < .05$, cluster size > 30 voxels) for BOLD-signal, CBF, and CMRO2. **B|** Histograms depict median voxel distributions across subjects of ΔBOLD, ΔCBF, and ΔCMRO2 (CALC minus CTRL) within the binarized CALC-positive and CALC-negative group masks (shown as surface plot). **C|** Subject distribution of ΔBOLD, ΔCBF, and ΔCMRO2 within individual native-space BOLD-fMRI masks of significant positive (orange) and negative (blue) BOLD responses. Dots represent subject-specific parameter values, calculated as the median across voxels within individual masks. Paired samples t-tests, ** $p < .001$. Gray lines connect values obtained from individual subjects, red lines indicate subjects where the sign of ΔCBF and ΔCMRO2 deviates from the expected direction. **D|** Regional clusters (designate by numbers) of positive and negative BOLD responses (PLS group results, thresholded at BSR > ±3) and associated bar plots illustrate ΔCBF and ΔCMRO2. Please note the different axes for ΔBOLD versus ΔCMRO2. Bars indicate ΔCBF[%] and ΔCMRO2[%] median across voxels, error bars 95% CI, 2000 bootstraps. Signal increases and decreases that result in error bars crossing the zero line are considered non-significant. Clusters are located in different functional networks, as depicted on the brain surface and in axial slices (Yeo et al., 2011): visual (VIS); dorsal attention (DAN); frontoparietal (FPN); ventral attention (VAN); somatomotor (SMN); default mode (DMN) network.

In the next step, we conducted identical analyses to compare CALC with the REST baseline (Fig. S1A). Across subjects, we observed stronger ΔBOLD in both directions compared to REST than compared to CTRL (Fig. S1B). Nonetheless, the discrepancy between the sign of ΔBOLD and ΔCMRO2 persists, as there were significantly positive ΔCBF and ΔCMRO2 in CALC-positive masks, but only weakly negative ΔCBF and negligible ΔCMRO2 in CALC-negative masks across subjects (Fig. S1B).

Finally, the MEM task provides the opportunity to examine changes in quantitative parameters within brain regions similar to those observed in the CALC-negative task, but this time expecting positive responses (Fig. S1C). For MEM vs CTRL, we observed the majority of positive ΔBOLD in the DMN (Fig. S1E). Across subjects, ΔBOLD exhibits an overall range similar to CALC vs CTRL, again with a higher amplitude of positive than negative ΔBOLD (Fig. S1F). Once again, ΔCBF and ΔCMRO2 are only significant within positive, but not within negative ΔBOLD masks.

A summary of the average changes observed across subjects for all parameters and all task contrasts is presented in Table 2. Collectively, we found a significant overall coupling of positive ΔBOLD-ΔCMRO2 in different task conditions and when compared to different baseline states. However, the strength of positive coupling varied across regions (Fig. 2D). Importantly, we did not observe any significant decrease in oxygen metabolism in any BOLD-negative region.

Table 2

Mean BOLD signal change and parameter values across subjects (standard deviation) within individual BOLD-fMRI masks, separately for positive and negative BOLD responses.

task baseline	**BOLD mask**	**BOLD** [%]	**CBF** [ml/100g/min]		**CMRO2** [μmol/100g/min]		**OEF** [ratio]	
			baseline	ΔCBF	baseline	ΔCMRO2	baseline	ΔOEF
CALC CTRL	CALC-pos	**0.67%**	46.7 (8.3)	**7.9%** 3.2** (3.2)	123.9 (20.2)	**5.1%** 6.0** (7.8)	0.37 (0.05)	**-3.6%** -0.013** (0.01)
	CALC-neg	**-0.41%**	46.0 (6.7)	-1.8% n.s.	121.1 (17.3)	0.41% n.s.	0.35 (0.05)	1.0% n.s.
MEM CTRL	MEM-pos	**0.61%**	48.7 (9.0)	**5.6%** 2.6** (2.8)	124.9 (17.8)	**5.4%** 6.4** (8.2)	0.36 (0.05)	**-0.8%** -0.003* (0.013)
	MEM-neg	**-0.44%**	48.4 (8.9)	-1.8% n.s.	125.4 (29.5)	-1.0% n.s.	0.35 (0.06)	1.2% n.s.
CALC REST	CALC-pos	**0.94%**	45.6 (8.9)	**9.4%** 4.4** (3.2)	122.7 (23.6)	**6.6%** 6.8** (8.2)	0.38 (0.05)	**-3.9%** -0.015** (-0.013)
	CALC-neg	**-0.48%**	47.9 (7.9)	**-2.22%** -1.0* (3.5)	123.0 (19.3)	0.45% n.s.	0.35 (0.05)	1.4% n.s.

Note. Quantitative values (black) of CBF, CMRO2 and OEF are displayed both at baseline and as delta values (task minus baseline), along with percent change values (colored) for each contrast. Values reflect data as displayed in Fig. 2, with CMRO2 values in CALC being corrected for CBV increases, see Methods. ** $p < .001$, * $p < .05$, based on paired t-tests, df=39 for CALC vs CTRL contrasts, df=29 for CALC vs REST and MEM vs CTRL contrasts.

Control analyses

According to the hemodynamic response model (Fig. 1D), changes in CBF are the main contributor to the neurovascular coupling mechanism. Therefore, we performed several control analyses to ensure the regional and temporal integrity of our CBF data (Fig. S2).

First, we identified magnitudes of ΔCBF ranging from -12% to +29%, which aligns with previous reports of regional ΔCBF during cognitive processing (Fig. S2A, see Methods). Second, regions with positive ΔCBF exhibited a higher *n*-ratio compared to regions with negative ΔCBF (Fig. S2A, scatter plot). Third, our pattern of negative ΔCBF during CALC corresponds to the localization of CBF reductions observed with positron-emission tomography (PET) during various cognitive tasks (Fig. S2B). It is worth noting that CBF decreases are generally less widespread than BOLD signal decreases (Fig. S2B, comparison of group PLS results for BOLD and CBF) and predominantly centered around the peaks shown in Fig. S2A.

Subsequently, we assessed the temporal stability of BOLD and CBF signals during measurement blocks that lasted several minutes. In the primary experiment (Fig. 1), we used different block durations for BOLD and quantitative fMRI in order to optimize the signal-to-noise ratio for each modality. To this end, we collected BOLD fMRI data from a separate group of participants (N=18) who performed the CALC and MEM tasks in continuous 3-minute blocks. Fig. S2C demonstrates that the temporal profiles within individual BOLD masks remained constant throughout the entire duration of the task, indicating the absence of habituation effects. Additionally, the average amplitudes of ΔBOLD were similar to those observed in our main study (CALC-positive/CALC-negative/MEM-positive, ΔBOLD[%]: 0.6/-0.46/0.34; main study: 0.67/-0.41/0.61). Finally, the time-resolved analysis of CBF signals from the main experiment shows that the signal fluctuations remain stable throughout the entire measurement blocks (Fig. S2D).

Thus far, our findings suggest that quantitative fMRI is capable of measuring individual parameters of neurovascular coupling across the entire cortex in healthy individuals, particularly quantitative CBF and CMRO2 in baseline and task conditions. On average, CBF and CMRO2 increase in regions exhibiting significant positive ΔBOLD, but with regional variations. However, significant negative ΔBOLD does not indicate absolute decreases in metabolism, neither on the level of voxels nor regions. Importantly, discordances between BOLD and CMRO2 responses are not limited to specific regions, such as the DMN, but also occur in networks and regions with positive ΔBOLD (see Fig. 2D for regional variability of positive and negative ΔBOLD-ΔCMRO2 coupling).

Empirical validation of the Davis model explaining concordant and discordant BOLD responses

In the subsequent section, we elaborate upon the hemodynamic mechanisms that may be responsible for the discrepancies between ΔBOLD and underlying metabolic activity. The Davis model (Davis et al., 1998) has been established to formalize the dependence of a realistic range of ΔBOLD amplitudes on the *n*-ratio, which represents the relationship between ΔCMRO2[%] and ΔCBF[%] (as depicted in Fig. 3A). When ΔCBF surpasses ΔCMRO2, one observes the canonically expected BOLD response, with ΔBOLD, ΔCBF, and ΔCMRO2 all changing in the same direction. However, ΔBOLD may also disagree with the actual metabolic changes if ΔCBF is lower than ΔCMRO2, i.e. for an *n*-ratio <1, or if ΔCBF and ΔCMRO2 show opposing signs. These areas of discordance between ΔBOLD and ΔCMRO2 are indicated by violet shadings in Fig. 3A.

For instance, one would measure a negative ΔBOLD of -1.3% for a strong increase in metabolism of +20%, if CBF increases by only around 5%. In other words, the same ΔCMRO2 value can lead to opposite signs of ΔBOLD, depending on the extent of ΔCBF. Since we measured ΔBOLD, ΔCBF and ΔCMRO2, our data are ideally suited to investigate the validity of the Davis model.

Fig. 3B presents empirical data of ΔCBF versus ΔCMRO2, colored by ΔBOLD, across all gray matter voxels of the cortex for CALC vs CTRL (see also Fig. S3A for CALC vs REST, and Fig. S4A for MEM vs CTRL). In order to mitigate SNR issues when integrating all imaging modalities on the voxel level, we employed semi-quantitative calculations of CMRO2 (see Methods and Fig. S5). Our experimental data substantiate several predictions of the Davis model. Voxels exhibiting positive and negative ΔBOLD group above and below a straight line, respectively, with an approximate incline of 1. Thus, voxels showing negative and positive ΔBOLD align within the predicted segments of the Davis model. Importantly, the plot also confirms a significant number of voxels with discordant BOLD responses, illustrated by red voxels on the left and blue voxels on the right side of zero ΔCMRO2 (red dashed line). Based on BOLD-fMRI data alone and relying on their canonical interpretation, the activity in those voxels would be misinterpreted.

To provide a clearer illustration of the discordance between ΔBOLD and ΔCMRO2 at the voxel level, we split the data from Fig. 3B into two distinct scatter plots for CALC-positive (upper row) and CALC-negative (lower row) contrasts (Fig. 3C). In both plots, voxels with discordant ΔBOLD compared to ΔCMRO2 were highlighted by violet shading. The number of discordant voxels amounted to 30% and 66% for positive and negative ΔBOLD, respectively (Fig. 3C, pie charts). The second pie chart in the lower scatter plot demonstrates a similar ratio of discordant voxels when only including negative ΔBOLD voxels within the DMN. Furthermore, the brain slices demonstrate that discordant voxels are distributed spatially across all clusters or regions of the cortex (Fig. 3C, Spatial distribution). The stacked bar plots reveal that discordant voxels are equally distributed among voxels with the lowest to highest quartile of BOLD signal amplitudes (Fig. 3C, BOLD amplitude distribution, q1 represents the lowest quartile and q4 represents the highest quartile of BOLD signal amplitudes).

We conducted the same analyses for the CALC vs REST (Fig. S3B) and MEM vs CTRL (Fig. S4B) tasks. Across these additional contrasts, we likewise observed the presence of discordant voxels across the entire range of ΔBOLD. Here, the ΔBOLD positive and negative discordant voxels accounted for 33% and 50% of all significant voxels in the CALC vs REST contrast, and 14% and 53% in the MEM vs CTRL contrast. Again, discordant voxels were distributed throughout the entire cortex.

In summary, a considerable number of voxels within patterns of significant positive and negative ΔBOLD exhibit an inverse ΔCMRO2 (Fig. 3D, violet bars). The cause for this discordant BOLD response is a lower ΔCBF than what would be anticipated from the canonical hemodynamic response model with an *n*-ratio >1. Importantly, discordant ΔBOLD occurs in one-third of voxels with positive ΔBOLD and in two-thirds of voxels with negative ΔBOLD. Interestingly, voxels with discordant ΔBOLD are uniformly dispersed throughout the cortex and arise within all ranges of ΔBOLD magnitudes. In the next section, we investigated whether this variability in hemodynamic and metabolic responses during task processing might relate to differences in hemodynamics during baseline states.

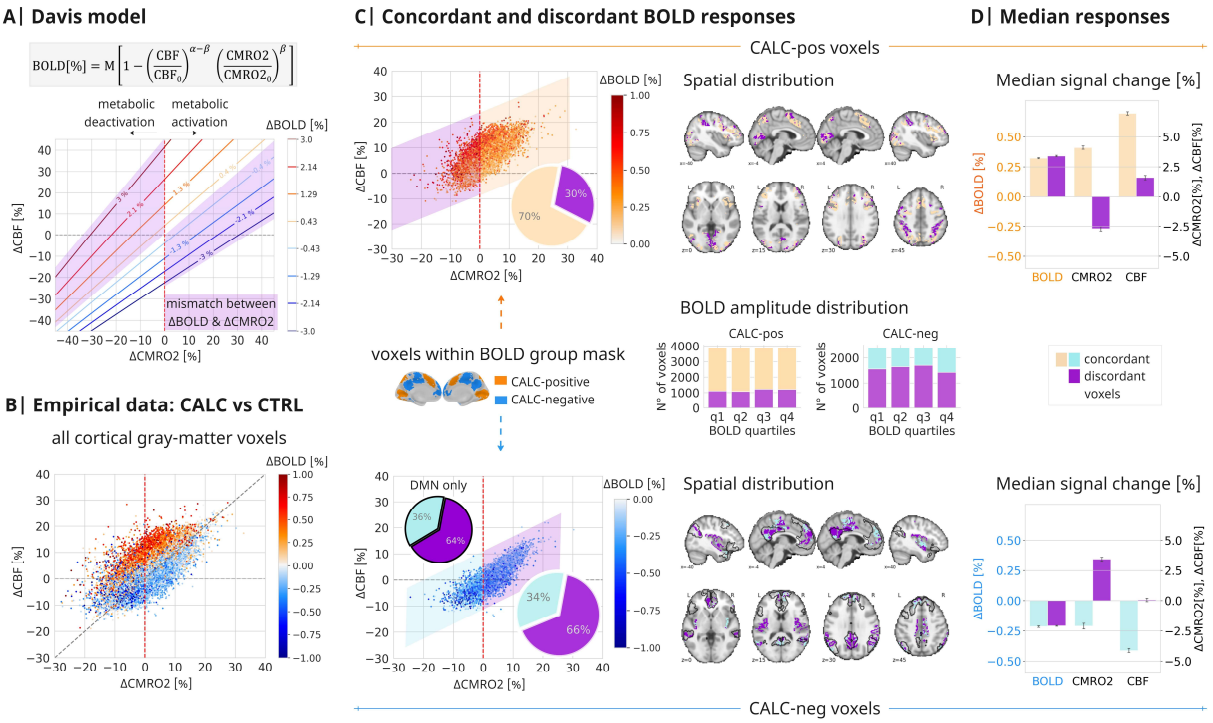

Figure 3. Dependence of BOLD responses on changes in CBF and CMRO2. A| Visualization of the Davis model. Predicted BOLD responses (ΔBOLD[%]) are depicted as colored contour lines in relation to ΔCBF[%] and ΔCMRO2[%]. The model illustrates that the sign and amplitude of the BOLD response depend on the amplitudes of ΔCBF[%] and a given ΔCMRO2[%]. The canonical hemodynamic response model requires that ΔCBF surpasses ΔCMRO2, resulting in a positive ΔBOLD, and vice versa for negative ΔBOLD. However, the Davis model predicts a range of BOLD responses with discordant signs compared to the change in underlying metabolic activity (violet shading). **B|** Empirical data from BOLD- and quantitative fMRI for all cortical voxels. ΔCMRO2, as required by the Davis model, was calculated from semi-quantitative data (see Methods), median across all subjects per voxel, colors indicate ΔBOLD[%]. Our experimental data replicate the slope and range of values as predicted by the Davis model, particularly demonstrating a substantial number of voxels with ΔBOLD opposing ΔCMRO2. **C|** Voxels with significantly positive (upper row) and negative (lower row) BOLD responses, extracted from (B), are plotted separately. Voxels with ΔBOLD concordant to ΔCMRO2 are depicted in pale, while voxels with discordant ΔBOLD are depicted in violet color. The pie plots summarize the ratio of discordant to concordant voxels. In the lower panel, the pie plot with black contours summarizes the ratio of discordant voxels within only the DMN. Axial slices illustrate the spatial distribution of significant concordant and discordant BOLD voxels, with black contours depicting the DMN. The stacked bars in the right center depict the amplitude distribution of discordant and concordant voxels across BOLD amplitude quartiles. It is noteworthy that discordant voxels show neither spatial nor amplitude preference. **D|** The bar plots show median ΔCMRO2[%] and ΔCBF[%] across all voxels with either concordant or discordant ΔBOLD[%], error bars = 95% CI, 2000 bootstraps. Please note that discordant and concordant voxels feature a similar ΔBOLD amplitude distribution.

Baseline OEF and vasculature architecture correlate with different types of hemodynamic responses

First, we pooled all voxels with significant ΔBOLD across tasks, which amounted to 53% of all grey matter voxels, and separated them into voxels displaying concordant versus discordant BOLD changes (Fig. 4A, pie chart). Subsequently, we examined the voxel-wise relationship

between CMRO2 and CBF, OEF, and CBV during CTRL baseline. We found a significant linear relationship for each of the three hemodynamic parameters, consistent across voxels of all three pools (Fig. 4A). Next, we used multiple linear regression to identify the individual contribution of OEF, CBF, or CBV to the variance of CMRO2 during baseline. The overall regression was statistically significant across both concordant and discordant voxels (concordant model: $F(3,22154) = 71790$, $p < .001$, CMRO2 = 139.4 + 318.8*OEF + 3.3*CBF + 0.4*CBV + e, R^2=0.91; discordant model: $F(3,14333) = 47320$, $p < .001$, CMRO2 = 128.6 + 311.5*OEF + 3.2*CBF + 1.6*CBV + e; R^2=0.91; all predictors mean-centered, *p*<.001 for all beta values). Importantly, the OEF contributes most to CMRO2 variance during baseline (concordant/discordant, relative explained variance: 70%/68%), followed by CBF (29%/30%), and CBV (1%/3%).

Next, we assessed whether pools of concordant and discordant voxels differ in average CBF, OEF, and CBV during baseline. Across subjects, discordant voxels showed, on average, significantly lower CBF, lower OEF, and higher CBV in CTRL than concordant voxels (Fig. 4B). We replicated our finding of lower OEF and higher CBV with two external, high-resolution imaging datasets from quantitative susceptibility mapping (QSM) of the human brain (Fig. 4C). In discordant voxels, we found lower susceptibility, indicating lower dHB content (upper bars) in the first dataset (Huck et al., 2019), and higher venous density (lower bars) in the second dataset (Lüsebrink et al., 2021).

In summary, this suggests that baseline OEF relates best to baseline CMRO2 across the entire human cortex. Furthermore, voxels with discordant ΔBOLD during tasks possess lower OEF and a higher CBV during baseline, which may relate to a distinct vascular architecture within those voxels.

Does the difference in baseline hemodynamics and oxygen metabolism impact the hemodynamic changes during task conditions? Indeed, we identified two different modes of hemodynamic responses for concordant and discordant voxels across all tasks (Fig. 4D). In accordance with the canonical hemodynamic model, concordant voxels modulate ΔCMRO2 primarily via ΔCBF. A multiple linear regression confirms the significant contribution of ΔCBF and ΔOEF to the voxelwise variance of ΔCMRO2 ($F(2,22319) = 65810$, $p < .001$), with ΔCBF explaining 87% and ΔOEF 13% of a total explained variance of R^2=0.86 of the model (ΔCMRO2[%] = 2.6 + 0.88*ΔOEF[%] + 0.88*ΔCBF[%] + e; all predictors mean-centered, *p*<.001 for all beta values). Intriguingly, discordant voxels show a different form of hemodynamic response driven by ΔOEF. As shown in the scatterplots in Fig. 4D and confirmed by the multiple linear regression ($F(2,14480) = 35130$, $p < .001$), ΔOEF explains 65% and ΔCBF 35% of a total explained variance of R^2=0.83 of the model (ΔCMRO2[%] = 1.1 + 1.1*ΔOEF[%] + 0.85*ΔCBF[%] + e; all predictors mean-centered, *p*<.001 for all beta values). Hence, ΔCMRO2 is predominantly regulated by ΔCBF in concordant and by ΔOEF in discordant voxels. As empirical ΔCBV only exists for the CALC-CTRL contrast it was left out of the regression models explaining ΔCMRO2. Furthermore, it should be noted that the negative correlation between ΔCMRO2 and ΔOEF (Fig. 4D, middle plot) reflects the compensatory rise in oxygen levels with excessive ΔCBF in concordant voxels.

We here identified a second type of hemodynamic response in a substantial number of voxels during task engagement. However, the type of hemodynamic response might also be related to the type of task or any other aspect inherent to each voxel that we haven't considered so far. In a final step, we therefore investigated whether baseline OEF predicts the hemodynamic response type within the same voxel and irrespective of the task condition. In a conjunction

analysis of all tasks, we identified 4099 voxels exhibiting significant ΔBOLD in both directions during either CALC or MEM (Fig. 4E, pooled voxels). We then labeled each voxel according to whether it exhibits either consistent OEF- or CBF-driven responses during MEM and CALC, or whether the response differed in the two conditions (Fig. 4E, orange voxels). The pie chart illustrates that the majority of voxels (47%) showed a mixed response being either OEF- or CBF-driven, while 19% and 34% showed a consistent OEF- and CBF-driven response, respectively. Even though the response type is not strictly dependent on the type of cognitive task (mixed responses: 69% discordant during CALC, 31% discordant during MEM), we identified a significantly higher baseline OEF in voxels with mixed response (0.37) compared to those with OEF-driven response (0.31). The highest baseline OEF (0.42) occured in consistently concordant voxels regulating task response consistently via ΔCBF (Fig. 4E, violin plots).

In summary, we identified two possible modes of hemodynamic responses to changes in neuronal activity and metabolism. In particular, we revealed that the response type depends on the baseline OEF in a given voxel. Voxels with lower baseline OEF regulate task demands with an OEF-driven hemodynamic response, while voxels with the highest baseline OEF regulate task demand via ΔCBF. Thereby, the level of baseline OEF seems to relate to differences in voxel vasculature. Critically, only around one third of all voxels in our subsample consistently relied on ΔCBF during task response irrespective of the sign of ΔBOLD.

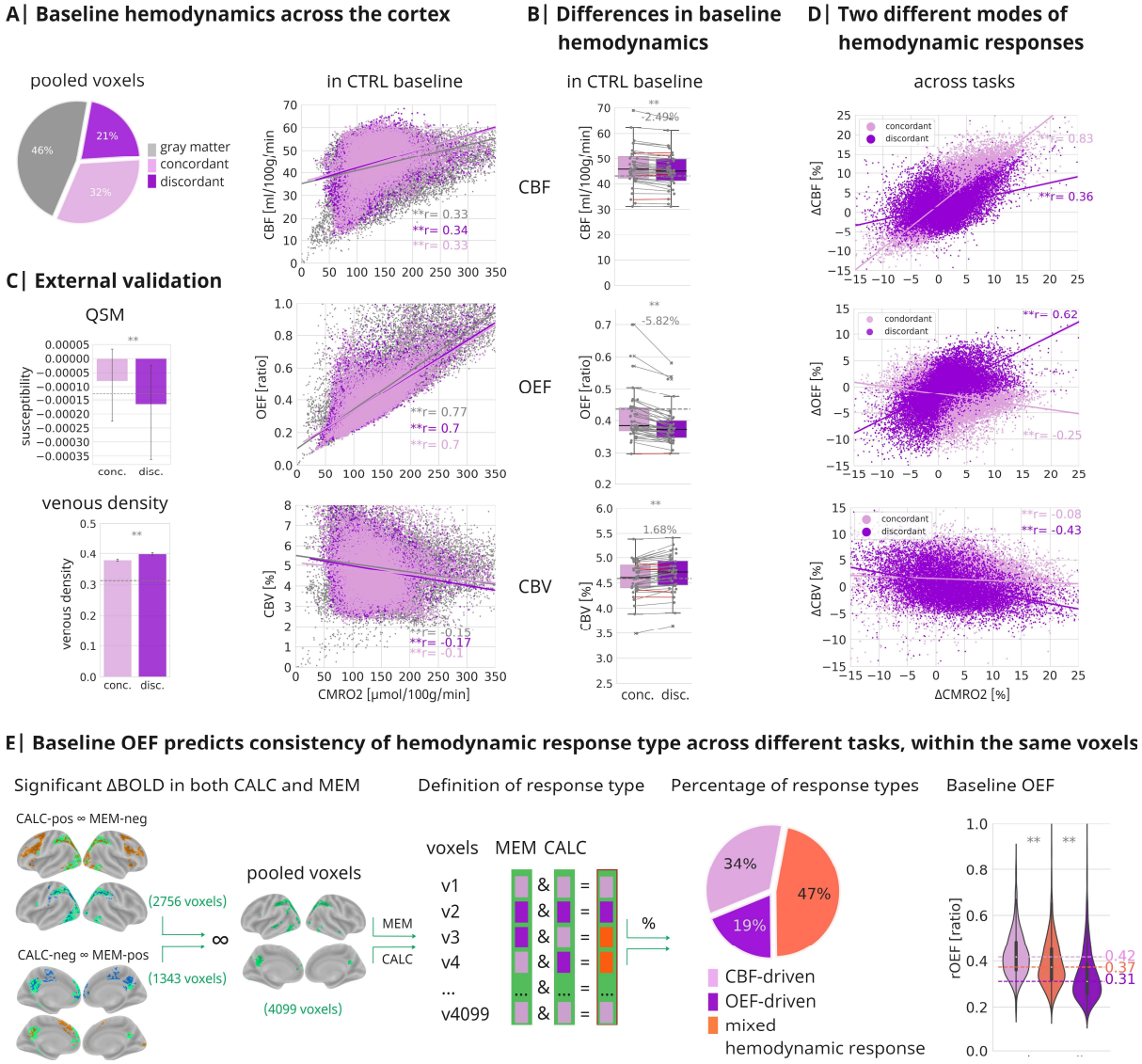

Figure 4. Two modes of CMRO2 regulation, via CBF or OEF. A| Regulation during CTRL baseline. Across all gray matter voxels and all task conditions, 21% showed discordant and 32% showed concordant responses. During baseline, CMRO2 and OEF were highly correlated, Pearson's $r > 0.7$, $p < .001$ for each pool of voxels. CMRO2 and CBF showed a medium correlation ($r > 0.32$, $p < .001$), and CMRO2 and CBV showed a weak negative correlation ($r < -0.1$, $p < 0.01$) across all groups of voxels. **B|** Across subjects, discordant voxels, on average, show significantly lower CBF (-2.49%), OEF (-5.82%), and higher CBV (1.68%) than concordant voxels, paired-samples t-test, $p < .001$. Boxplots: line, median; box limits, upper and lower quartiles; gray line, median of remaining GM voxels. **C|** Lower negative baseline susceptibility (QSM) and higher venous density in discordant vs concordant voxels, as revealed by two external datasets (Huck et al., 2019; Lüsebrink et al., 2021). Bar plots: error bars = 95% CI, 2000 bootstraps. ** $p < .001$, independent samples permutation test on the median values, conducted for discordant versus concordant voxels, 2000 permutations. **D|** Correlation of ΔCMRO2[%] with either ΔCBF[%], ΔOEF[%], or ΔCBV[%], across all task contrasts (CALC or MEM vs CTRL), separately for concordant (pale) and discordant (dark violet) voxels. ΔCMRO2 and ΔCBF showed a strong positive correlation across concordant voxels ($r = .83$, $p < 0.01$), and a weak correlation across discordant voxels ($r = .36$, $p < .001$). On the contrary, ΔCMRO2 and ΔOEF showed a moderate, positive correlation across discordant voxels ($r = .62$, $p < .001$), and a weak, negative correlation across concordant voxels ($r = -.25$, $p < .001$). ΔCBV could only be calculated for a subset of 10 subjects, and only across the CALC vs CTRL contrast, see Methods. ΔCMRO2 and ΔCBV across this subset showed a weak correlation around zero

across concordant voxels correlation (r = -.08), and a moderate, negative correlation across discordant voxels (r = -.43, p < 0.001). **E|** Conjunction voxels (green outlines) that showed either positive ΔBOLD during CALC and negative ΔBOLD during MEM (upper row) or vice versa (lower row) were pooled and the overall response type of each voxel was identified. 34% of all voxels showed concordant responses (same sign of ΔBOLD and ΔCMRO2) during both MEM and CALC conditions, while 19% of voxels showed discordant responses during both tasks. For 47% of voxels, the hemodynamic response was CBF-driven during one, and OEF-driven during the other task. Violin plots show a significant difference in baseline OEF averaged across voxels of either response type. Voxels with the highest baseline OEF regulate task demand in a CBF-driven hemodynamic response, while voxels with the lowest baseline OEF rely predominantly on an OEF-driven response. ** p < .001, independent samples permutation test on the median values, conducted for mixed versus other voxel types, 2000 permutations.

DISCUSSION

The present study investigated how reliably BOLD responses during task processing reflect changes in oxygen metabolism across the cortex. During two different task conditions, more than 50% of all gray matter voxels exhibited either significant positive or negative ΔBOLD. Among those, 60% displayed metabolic changes in line with predictions of the canonical hemodynamic response model (Fig. 4A). Intriguingly, for the remaining 40% of voxels, the changes in CMRO2 were found to be discordant with the canonical interpretation of ΔBOLD, whereby negative ΔBOLD was associated with increased oxygen metabolism and positive ΔBOLD was associated with decreased oxygen metabolism. Voxels exhibiting a mismatch between ΔCMRO2 and ΔBOLD signals were observed across the entire cortex and during both task conditions. For voxels where we empirically identified BOLD responses during both task conditions, the ratio of voxels showing the canonical hemodynamic response with surplus ΔCBF dropped to around one-third of voxels with significant ΔBOLD. Our results suggest that the reason for the mismatch between ΔBOLD and ΔCMRO2 is a different hemodynamic response than anticipated by the canonical model. Instead of regulating changes in oxygen demand via changes in CBF, oxygen demand is covered directly via OEF. We found that OEF-regulating voxels show a lower OEF during baseline conditions and a higher vascular density. We speculate that these voxels might have a greater 'oxygen buffer', thereby avoiding the need to regulate oxygen supply via changes in CBF.

To obtain voxel-level measures of CMRO2, we employed a gas-free, multiparametric quantitative BOLD MRI protocol (Christen et al., 2012; He & Yablonskiy, 2007; Hirsch et al., 2014; Kaczmarz, Hyder, et al., 2020; Stone & Blockley, 2017). This quantitative fMRI technique has been successfully applied to patient cohorts to study vascular pathologies (Göttler et al., 2019; Kufer et al., 2022). To the best of our knowledge, we here used multiparametric, quantitative fMRI for the first time to examine the widespread metabolic effects in the human brain during different cognitive states. All quantitative parameter values obtained in this study fell within the range of previously reported data for the healthy human brain, with average values for CBF of 44.5 ± 7.2 ml/100g/min, CBV of 4.8 ± 0.2 %, OEF of 0.39 ± 0.04 [fraction], and CMRO2 of 127.8 ± 18.4 µmol/100g/min in the gray matter (Aoe et al., 2018; Cho et al., 2018; Gauthier & Hoge, 2012; Ito et al., 2021; Lee & Wehrli, 2022; Leontiev & Buxton, 2007; Liang et al., 2013; Raichle et al., 2001; Stone & Blockley, 2017; Wise et al., 2013; J. Zhang et al., 2015, 2015). Likewise, task-related percent changes for the different parameters (see Table 2) were similar to previous studies (Gauthier et al., 2012; Restom et al., 2008; Y. Zhang et al., 2021), and we observed n-ratios > 2 in regions with positive ΔCBF (Uludağ et al., 2004). This

concordance with previous studies confirms the reliability of quantitative fMRI for future investigations, particularly in the study of patient cohorts with potentially altered hemodynamics such as during aging (Tsvetanov et al., 2020) or in neurodegenerative disorders (Chen et al., 2022). In addition, we demonstrated that prolonged task processing over several minutes induces stable and persistent changes in hemodynamics specifically for CBF and BOLD signals (see Fig. S2). The fact that we replicated positive CBF responses within regions exhibiting significant BOLD increases (Kim 2006, Qihong Zou 2011, Jog 2016) and localized CBF decreases within the DMN in line with seminal work from Shulman et al. (Shulman, Corbetta, et al., 1997, S. 19) made us confident in our CBF measurements. As CBF decreases were much more localized than negative ΔBOLD clusters, they were not significant within larger regions of significant BOLD signal decreases.

The cognitive tasks that participants performed elicited the expected patterns of BOLD responses. Previous research has shown that externally oriented cognitive tasks, such as the CALC condition, induce positive ΔBOLD in somatosensory, frontoparietal, and ventral- and dorsal attention regions (Amalric & Dehaene, 2016; Fehr et al., 2007; Lin et al., 2011a) and a negative ΔBOLD in default mode regions (Anticevic et al., 2012; Raichle et al., 2001; Shulman, FIEZ, et al., 1997; Smallwood et al., 2021), while self-related, autobiographical memory tasks induce a positive ΔBOLD in DMN regions (Andrews-Hanna et al., 2014; Davey et al., 2016; Ino et al., 2011; Spreng & Grady, 2010). Commonly, the BOLD response in cognitive tasks is compared to experimentally controlled baseline conditions (Addis et al., 2007; Burianova et al., 2010; Burianova & Grady, 2007a; DuPre et al., 2016; Spreng et al., 2010; Spreng & Grady, 2010). However, studies on negative ΔBOLD often compare against uncontrolled resting-state (Anticevic et al., 2012; Lin et al., 2011a; Pfefferbaum et al., 2011; Raichle et al., 2001; Singh & Fawcett, 2008). Hence, we included both types of baseline conditions in our study. As expected, task effects of ΔBOLD were stronger when compared against undemanding REST, yet the discrepancies in sign and amplitude of ΔBOLD or ΔCBF and ΔCMRO2 were present for both baseline conditions and persisted in the region-specific analyses (Figs. 2D and S2A). A similar mismatch between amplitudes of ΔBOLD and hemodynamic or metabolic changes has been shown in animal data for the comparison between cortical and subcortical regions (Huo et al., 2014; Shaw et al., 2021b; Shih et al., 2011b).

To assess the heterogeneity of neurovascular coupling more accurately, we employed the Davis model as an explanatory approach. The Davis model formalizes the relationship between amplitudes of ΔBOLD and realistic ranges of ΔCMRO2 and ΔCBF (Davis et al., 1998). This model has predominantly served to calculate relative changes in CMRO2 from combined CBF and BOLD measurements in calibrated BOLD-fMRI studies (Blockley et al., 2012, 2013; Chen et al., 2022; Griffeth & Buxton, 2011). Interestingly, despite being published approximately two decades ago, no study has yet validated the model in humans by means of quantitative measurements of ΔBOLD, CMRO2 and CBF and likewise explored the extent of disparity between ΔBOLD and hemodynamics that the model incorporates (see Fig. 3, violet shadings). Indeed, across the entire cortex, our empirical data fit very well with the predicted distribution of concordant and discordant voxels as encompassed in the Davis model. By averaging quantitative parameter values across concordant voxels, we find ΔCBF and ΔCMRO2 as expected by the canonical hemodynamic model with an *n*-ratio of approximately 2 (Fig. 3D). However, the remaining 30% - 66% of discordant voxels exhibit ΔCBF much weaker than expected. The absence of sufficiently large CBF changes accounts for the discrepancy between BOLD signal and metabolic responses and reflects non-canonical hemodynamic responses that hamper the common interpretation of BOLD signal changes. Such a mismatch in neurovascular

coupling has previously been only reported for subcortical regions in rodents (Shaw et al., 2021b). Importantly, we find a ΔBOLD-ΔCMRO2 mismatch that manifests ubiquitously across the human cortex and across all magnitudes of BOLD amplitude changes.

Finally, we showed that the weak ΔCBF in discordant voxels depends on their baseline physiologic state (Fig. 4). Upon aggregating concordant and discordant voxels across all task contrasts, we found that discordant voxels generally exhibit significantly lower CBF, higher CBV, and, most prominently, lower OEF in comparison to concordant voxels. Importantly, we were able to confirm these differences in baseline OEF and CBV using external data obtained from quantitative susceptibility mapping (Huck et al., 2019; Lüsebrink et al., 2021) (Fig. 4C). In general, OEF was the most robust predictor for the variation in baseline CMRO2 across all cortical voxels. Based on these results, we identified two different response types for ΔCMRO2 across tasks. Concordant voxels cover changes in CMRO2 mostly via CBF, discordant voxels predominantly via ΔOEF (Fig. 4D). In principle, our findings align well with rodent data showing that, as the vascular composition varies, diverse patterns of neurovascular coupling might emerge (Ances et al., 2008; Boorman et al., 2010; A. Ekstrom, 2010; Shaw et al., 2021b).

Thus far, we compared positive or negative ΔBOLD located in different cortical areas. As a final step, we identified a set of voxels exhibiting both directions of BOLD responses across the two tasks. This enabled us to investigate whether task type or inherent vascular characteristics of a given voxel were possibly responsible for the discordant BOLD response. We demonstrate that the consistency of either concordant or discordant ΔBOLD across tasks seems to be related to significant differences in baseline OEF. Voxels with highest baseline OEF regulate metabolic demands by ΔCBF, while voxels with lower OEF during baseline serve increased metabolic demands through higher OEF. This suggests that voxels with lower baseline OEF have a higher oxygen buffer, which allows them to cover changes in oxygen demand during task conditions via ΔOEF; especially increased oxygen demand is simply covered by increasing OEF, making it not yet necessary to rely on compensatory flow mechanisms during task conditions.

In summary, we have identified an OEF-driven type of hemodynamic response in a substantial volume of the human cortex that, most critically, reverses the direction of the metabolic interpretation of BOLD signal changes. Apart from the conventional hemodynamic response with ΔCBF surpassing ΔCMRO2, approximately 40% of all voxels with significant ΔBOLD support metabolic demand through ΔOEF without significant changes in blood flow. Further, we identified higher CBV and lower OEF in the baseline state as a possible explanation for this phenomenon. This has several potential implications. Firstly, voxels regulating predominantly via OEF seem to possess a greater oxygen buffer, meaning that the oxygen pressure remains sufficiently high during task engagement (Leithner et al., 2010; Leithner & Royl, 2014). Secondly, the OEF-based hemodynamic response may relate to distinct signaling mechanisms, other than those inducing surplus ΔCBF, such as astrocytic activity (Takata et al., 2018), shifts in excitatory/inhibitory signaling (Buxton et al., 2014; Uhlirova et al., 2016), or neuromodulatory regulation (Koush et al., 2021). Thirdly, and irrespective of the underlying reason for the different hemodynamic responses during tasks, our findings indicate that the common interpretation of positive ΔBOLD as increased neuronal activity and negative ΔBOLD as decreased neuronal activity may not withstand across the entire human cortex. Using different task conditions, we induced significant ΔBOLD in approximately 50% of gray matter voxels, of which around 40% exhibited discordant BOLD responses, regulating metabolic demand through changes in OEF instead of CBF. For a subset of voxels showing ΔBOLD in both directions, we even showed that only one-third of voxels consistently regulate metabolic

changes via ΔCBF as assumed by the canonical hemodynamic response. This indicates that a reliable interpretation of neuronal activity in fMRI voxels actually requires quantitative fMRI or, as a minimum, additional measurements of ΔCBF to distinguish between the two types of hemodynamic responses.

METHODS

Subjects

We acquired data from 47 healthy subjects for our main study, seven of whom had to be excluded because of a) apparent behavioral task difficulties (n=1), b) problems with contrast-agent application (n=2), or c) data quality problems (severe motion artifacts in CBF or R2' data, unilateral CBF data in one condition, huge susceptibility artifacts) (n=4). Resting-state (REST) data from a subset of 16 subjects were already used for another publication (Kufer et al., 2022). For the the two main tasks, calculation (CALC) and control (CTLR), imaging data were acquired from 40 healthy subjects (22 women, 18 men; mean age 32.1 ± 9.2y, all right-handed). Additional data during autobiographical memory (MEM) and eyes-open, resting-state baseline (REST) were acquired from a subset of 30 subjects (17 women, 13 men, mean age 32.2 ± 9.6y). The control study (stability of BOLD-fMRI) was performed on a separate cohort of 18 healthy subjects (11 women, 7 men; mean age 28.1 ± 5.0y, all right-handed). All participants gave informed written consent to procedures approved by the Ethics Review Board of the Klinikum Rechts der Isar, Technical University of Munich.

Task design

Participants were lying in the scanner in a supine position and watched the task instructions on a screen behind the scanner via a mirror mounted on the head coil. Right hand responses were collected via a button box. Before entering the scanner, we explained the tasks to the participant, with an emphasis on staying concentrated and giving correct responses rather than being fast, and they performed a short test-run on a computer outside of the scanning room.

The CALC condition was designed to evoke negative BOLD responses in the DMN and positive BOLD responses in a task-positive network including frontoparietal and dorsal attention networks (DAN). The CALC task was a self-paced, continuous arithmetic task with a maximum response time of 10 seconds so participants had to continuously engage in calculations, adapted from Lin and colleagues (Lin et al., 2011b). Specifically, a row of three numbers plus a question mark (n1, n2, n3, ?) is presented with the instruction to mentally fill in the missing number, based on the following rule: n2 - n1 = DIFF, n2 = n1+(1*DIFF), n3 = n2+(2*DIFF), therefore ? = n3+(3*DIFF). An exemplary row is 33 38 49 ?. Here, the difference between the first and the second number is 5 and 3*5 is 15, so the number in question is 64 (49 + 15). The participants had three response options each assigned to a button on the response box.

The autobiographical memory task was based on the task-design of Spreng and colleagues (DuPre et al., 2016; Spreng & Grady, 2010), where participants were asked to remember a specific event in the past. We aimed to match the visual input across all three tasks, thus using a written cue-word instead of a picture. Instructions were given to the participants to remember all details of any event in the past, which came to their minds, independent of how well it related to the cue-word. The cue-word was shown for a maximum of 15 seconds. To track the average time it took participants to remember an event, i.e., how easy it was for them to recover a memory, they were instructed to press the first button twice as soon as an event came to their minds. If they could not remember any event or any more details, they were instructed to press the second and third button after each other in order to trigger a new cue-word. We employed this instruction of double-button pressing to match the total number of button presses across all tasks.

The CTRL condition was a task with low-level cognitive and attentional demands, where a row of random letters was shown for a fixed interval between 5.9 and 8.9 seconds and the participants had to decide via button-press if the first letter was a vowel or not. We employed CTRL as an active baseline, with matched visual input and button presses compared to the CALC and MEM tasks. While studies investigating DMN activations usually employ a matched control task (Addis et al., 2007; Burianova et al., 2010; Burianova & Grady, 2007b), studies investigating DMN deactivations, i.e., negative BOLD responses, usually compare a goal-directed task to an uncontrolled, resting state baseline (Lin et al., 2011b; Pfefferbaum et al., 2011; Raichle et al., 2001). This is why we also acquired REST data in 30 subjects, where a white fixation cross was presented on a black screen and participants were instructed to fixate the cross throughout scanning.

Image acquisition and experimental procedure

MRI of the main study was performed on a 3T Philips Elition Ingenia MR scanner (Philips Healthcare, Best, The Netherlands. The control study was performed on a 3T Philips Ingenia MR scanner (Philips Healthcare, Best, The Netherlands), both using a 32-channel head coil. Multi-parametric, quantitative BOLD MRI included the following sequences:

A) Multi-echo spin-echo T2 mapping**,** only in CTRL; 3D gradient spin echo (GRASE) readout as described previously by our group (Kaczmarz et al. 2020). 8 echoes with even-spaced echo times (TE): TE1 = ΔTE = 16ms; TR=251; α=90°; voxel size 2x2x3.3mm^3; 35 slices (30 slices in 4 subjects); total acquisition time = 2:28min (for 35 slices)

B) Multi-echo gradient-echo T2* mapping, in all conditions; as described previously by our group (Hirsch et al., 2014; Kaczmarz, Hyder, et al., 2020). 12 echoes, TE1 = ΔTE = 5ms; TR=2229ms; α=30°; voxel size 2x2x3mm^3; gap 0.3mm; 35 slices (30 slices in 4 subjects). Correction for magnetic background gradients with a standard sinc-Gauss excitation pulse (Baudrexel et al., 2009; Hirsch & Preibisch, 2013); acquisition of half- and quarter-resolution data in k-space center for motion correction (Nöth et al., 2014); total acquisition time = 6:08min (for 35 slices).

C) Dynamic susceptibility imaging (DSC), in 30 subjects only during CTRL, in 10 subjects additionally during CALC; as described previously by our group (Hedderich et al., 2019). Single-shot GRE-EPI; EPI factor 49; 80 dynamics; TR = 2.0s; α=60°; acquisition voxel size 2x2x3.5mm^3; 35 slices (30 slices in 4 subjects). Injection of gadolinium-based contrast agent as a bolus after 5 dynamics, 0.1ml/kg, minimum 6ml, maximum 8ml per injection (i.e. 16ml for two injections in a row, corresponding to a full clinical dosage), flow rate: 4ml/s, additionally flushing with 25ml NaCl; total acquisition time = 2:49min (for 35 slices).

E) Pseudo-continuous arterial spin labeling (pCASL), in all conditions; following Alsop et al. (2015) and as implemented by our group (Göttler et al., 2019; Kaczmarz, Hyder, et al., 2020).Post-labeling delay 1800ms, label duration 1800ms; 4 background suppression pulses; 2D EPI readout; TE=11ms; TR=4500ms; α=90°; 20 slices (16 slices in one subject); EPI factor 29; acquisition voxel size 3.28x3.5x6.0mm^3; gap 0.6mm; 30 dynamics including a proton density weighted M0 scan; total acquisition time = 6:00min.

The BOLD fMRI task-localizer was acquired using single-shot EPI, EPI factor 43; voxel size = 3.0x3.0x3.0mm^3; FOV 192x192x127.8mm^3; TE=30ms; TR=1.2s; α=70°; 400 dynamic scans plus two dummy scans; 40 slices; SENSE-factor = 2; MB-SENSE-factor = 2; total acquisition time: 8:05min. For susceptibility correction, a B0 field map was acquired with two echoes; TR/TE1/TE2=525ms/6.0ms/9.8ms; 40 slices; parallel acquisition; α=60°; voxel size = 3.0x3.0.3.0mm^3; FOV 192x192x127.8mm^3; total acquisition time: 0:35s.

Additionally, a T1-weighted 3D MPRAGE pre- and post-gadolinium (TI/TR/TE/α = 100ms/9ms/4ms/8°; CS-SENSE-factor=7.5; 170 slices; FOV=240x252x170 mm^3; voxel size 1.0x1.0x1.0mm^3; acquisition time=2:05min) and T2-weighted 3D FLAIR (fluid-attenuated inversion recovery) image were acquired for anatomical reference and to exclude brain lesions (TR/TE/α = 4800/293/40°; CS-SENSE-factor=10; 140 slices; FOV=240x248.9x168 mm^3; acquisition voxel size 1.2x1.2x1.2mm^3; turbo spin-echo factor 170; inversion delay 1650ms; acquisition time=2:09min).

After giving informed written consent, a venous catheter was placed into the forearm by a medical doctor and blood samples were taken for measurements of hemoglobin, hematocrit (Hct) and creatinine values. Before delivery of the contrast agent through the venous catheter at the end of the scanning session, creatinine values were requested and contrast agent was only applied if creatinine values were in a normal range to ensure healthy kidney function. Arterial oxygen saturation was measured via a pulse oximeter (Nonin 7500FO, Nonin Medical B.V., The Netherlands).

For the 10 participants who only performed CTRL and CALC conditions, all sequences were acquired in one session. The 30 participants, who performed all four conditions, performed two consecutive scanning sessions on the same day. In the first block, which took around one hour, participants completed all task runs, i.e., all mqBOLD sequences except the DSC scan, in addition to an 8min BOLD fMRI localizer, designed as a 30s-block-design with four repetitions per condition. For 17 subjects, the localizer fMRI scan was included in the second block instead of the first block. During a 15-25min break, participants completed a memory questionnaire, where they had to indicate how easy they found it to remember concrete events of the MEM task (difficulty scale; 1='very easy', 2='rather easy', 3='rather difficult', 4='very difficult') and how detailed their memories were overall (concreteness scale; 1='very detailed', 2='rather detailed', 3='rather vague', 4='very vague'). On average, people scored 1.8 +/- 0.7 on the difficulty scale and 2.0 +/- 0.6 on the concreteness scale. This means that, on average, it was rather easy for the subjects to remember a concrete event, and the memory was rather detailed. This also matched with the reaction times: on average, it took participants only 2.5 ± 1s to remember an event. In the second session, which lasted 30min on average, a REST fMRI BOLD scan (not used in this study) along with a B0 scan and other structural scans (volumetric T2, MPRAGE, FLAIR, post-gadolinium MPRAGE, all used for basic clinical screening) were acquired. At the very end of the protocol and in the presence of a medical doctor, the contrast agent application for DSC MRI was performed via a venous catheter by means of a dedicated pump (Accutron MR, Medtron AG, Saarbrücken, Germany).

Within the independent control study cohort, we acquired fMRI BOLD data only, during CALC, MEM and CTRL conditions, as well as a MPRAGE scan. Task blocks were 3min long with 1min interleaved CTRL blocks, all tasks were repeated four times. This resulted in a 33min continuous fMRI block, and participants were lying in the scanner for around 40min.

Quantitative parameter calculation using mqBOLD

The calculation of the quantitative parameter maps was performed with in-house scripts in Matlab and SPM12 (Wellcome Trust Centre for Neuroimaging, UCL, London, UK). Fig.1 displays all steps and subject-averaged parameter maps, median across gray-matter, with artifact areas masked, for each subject and condition in native space. Quantitative T2 and T2* parameter maps were obtained by mono-exponential fits of the multi-echo spin and gradient echo data as described previously by our group (Hirsch et al., 2014; Kaczmarz, Hyder, et al., 2020; Preibisch et al., 2008). Correction for macroscopic magnetic background fields (Hirsch &

Preibisch, 2013) and motion correction were performed using redundant acquisitions of k-space center (Nöth et al., 2014). R2' maps were calculated via

$$R2' = \frac{1}{T2*} - \frac{1}{T2} \quad [1]$$

yielding the transverse, reversible relaxation rate that is dependent on the vascular dHb content (Blockley et al., 2013, 2015; Bright et al., 2019). However, confounds from uncorrectable strong magnetic field inhomogeneities at air-tissue boundaries, iron deposition in deep GM structures as well as white matter structure need to be considered (Hirsch & Preibisch, 2013; Kaczmarz, Hyder, et al., 2020). The cerebral blood volume (CBV) was derived from DSC MRI via full integration of leakage-corrected ΔR2*-curves (Boxermann, J.L., Schmainda, K.M., Weisskoff, R.M., 2006) and normalization to a white matter value of 2.5% (Leenders et al., 1990) as described previously (Hedderich et al., 2019; Kluge et al., 2016). From R2' and CBV parameter maps, the oxygen extraction fraction (OEF) was then calculated via the mqBOLD-approach (Christen et al., 2012; Hirsch et al., 2014; Yablonskiy & Haacke, 1994) as

$$OEF = \frac{R2'}{c \cdot CBV} \quad [2]$$

with $c = \gamma \cdot \frac{4}{3} \cdot \pi \cdot \Delta\chi_0 \cdot hct \cdot B_0$, the gyromagnetic ratio $\gamma = 2.675 \cdot 10^8\ s^{-1}\ T^{-1}$, the susceptibility difference between fully deoxygenated and oxygenated hemoglobin of $\Delta\chi_0 = 0.264 \cdot 10^{-6}$, the magnetic field strength $B_0 = 3T$ and the small-vessel hematocrit *hct*, which was assumed to be 85% of our empirically measured (large-vessel) hematocrit values of each subject (Eichling et al., 1975; Hirsch et al., 2014). CBF maps were calculated from pCASL data as in (Alsop et al., 2015) to calculate CBF from averaged, pairwise differences of motion-corrected label and control images and a proton-density weighted image.

Finally, for each subject and condition, we calculated CMRO2 in a voxel-wise manner by combining all parameter maps via Fick's principle:

$$CMRO2 = OEF \cdot CBF \cdot C_aO_2 \quad [3]$$

where C_aO_2 is the oxygen carrying capacity of hemoglobin and was calculated as $C_aO_2 = 0.334 \cdot Hct \cdot 55.6 \cdot O_2sat$, with O_2sat being the oxygen saturation measured by the pulse oximeter (Bright et al., 2019; Ma et al., 2020). CBF was upscaled by 25% to account for systematic CBF underestimation due to four background-suppression pulses (Garcia et al., 2005; Mutsaerts et al., 2014). All parameter maps of each individual subject were registered to the first echo of their multi-echo T2 data.

Estimation of a realistic CALC CBV surrogate

To be able to estimate CBV changes during CALC, we measured DSC data in our two main conditions, CALC and CTRL, in a subset of 10 subjects. These subjects received a full clinical dosage of contrast agent altogether. More than a full clinical dosage of contrast agent cannot be given in one session, so we could not acquire additional DSC data for the MEM and REST conditions. From these measurements we determined the percent CBV changes of the CALC versus the CTRL condition across gray-matter in subject space, averaged within 360 Glasser regions of interest (ROIs) (Glasser, 2016). We then calculated the median change per ROI across the 10 subjects. We used this ROI-wise map of average ΔCBV to estimate a realistic CBV surrogate map during CALC for the remaining 30 subjects, where only one CBV measurement was available. We also used this CBV map during the MEM condition. This two-step procedure allowed us to take at least surrogate ΔCBV into account, as CBV data are usually not available in other quantitative fMRI studies.

Semi-quantitative CMRO2 estimation

The estimation of CMRO2 maps relies on the combination of R2', CBV and CBF values, according to Eq. [3]. Due to unfavorable error propagation especially from R2' measurements (see appendix in (Kaczmarz, Göttler, et al., 2020), we also calculated semi-quantitative CMRO2 and OEF values from BOLD fMRI data using the approach of Fujita et al. (2006). This solution was only applied for baseline R2', OEF and CMRO2 mapping in the MEM and CALC conditions. Instead of calculating ΔR2' from quantitative R2' (multi-echo GE-based T2*) during task conditions, we approximated ΔR2' as

$$\Delta R2' = -\frac{\Delta S}{S_0}\frac{1}{TE \cdot R2'_0} \qquad [4]$$

with TE = 30ms, $R2'_0$ being the baseline R2', and $\frac{\Delta S}{S_0}$ the BOLD signal change, derived from the fMRI BOLD localizer. R2' in CALC and MEM was then calculated via $R2' = R2'_0 + (\Delta R2' \cdot R2'_0)$ and OEF and CMRO2 were calculated according to Eqs. [2] and [3]. This approach was also repeated using data from the REST baseline. Thus, semi-quantitative compared to fully quantitative CMRO2 values in CALC and MEM conditions only differed in their usage of ΔR2' values, inferred from BOLD fMRI signal changes instead of fully quantitative task R2'. In Fig. S5, we directly compare results from the fully and semi-quantitative approach.

Davis model

The Davis model was inspired by numerical BOLD signal simulations and describes how changes in the BOLD signal depend on changes in CBF, CMRO2, relying on M, α and β (Davis et al., 1998):

$$\frac{\Delta S}{S_0} = M\left[1 - \left(\frac{CBF}{CBF_0}\right)^{\alpha-\beta}\left(\frac{CMRO2}{CMRO2_0}\right)^{\beta}\right] \qquad [5]$$

where α is a power-law exponent, relating CBV to CBF changes, and β is dependent on the microvascular anatomy (Bright et al., 2019). Previously, α = 0.38 was used, (Grubb et al., 1974) but more recently much lower values were determined. In our study, we used optimized parameters derived from rodents and simulations (Gagnon et al., 2016) with α = -0.05 and β = 0.98, as proposed for measurements on a 3T scanner with TE = 30ms. M is commonly referred to as the maximum BOLD signal change that would occur if all dHb was washed out of the vessels; it is dependent on the baseline physiology and OEF in baseline (Blockley et al., 2013). The Davis model was originally conceived for the calibration of fMRI experiments. To this end, M is estimated via combined measurement of CBF and BOLD responses to a vasoactive stimulus, mostly hypercapnia. By assuming α and β, fractional change in CMRO2 can be calculated from combined BOLD signal and CBF measurements (Blockley et al., 2013; Chen et al., 2022; Germuska & Wise, 2019). We did not use the Davis model to estimate changes in CMRO2, but compared its predictions for a range of realistic CBF, CMRO2 and BOLD changes to our empirical data.

BOLD- fMRI processing and task analysis

The BOLD fMRI localizer data were pre-processed using fMRIPrep 20.2.4 (Esteban, 2019) in a docker container, which is based on Nipype 1.6.1 (Gorgolewski et al., 2011). This included segmentation, estimation of motion-parameters and other confounds, susceptibility distortion correction, co-registration in native T1w space and normalization to MNI152 ICBM 2mm Non-linear 6th Generation Asymmetric Average Brain Stereotaxic Registration Model (Montreal

Neurological Institute, McGill University). FMRIPrep relies on FSL 5.0.9 (Jenkinson et al., 2012; Smith et al., 2004) with boundary-based registration (BBR) to register BOLD fMRI EPI time series to T1w data, FSL FAST for brain tissue segmentation and spatial normalization to standard space using ANTs 2.3.3 (Avants et al., 2008) registration in a multiscale, mutual-information based, nonlinear registration scheme, concatenating all transforms and applying all registration steps at once. This final normalization matrix was then applied to all quantitative mqBOLD parameter maps, after transforming all images to MNI 2mm standard space using 6-dof (degrees of freedom) co-registration to native T1w space. Further, as a control for partial least squares analysis described below, classical general linear model (GLM) task-analysis was implemented following recommendations in (Esteban et al., 2020).

We set up a GLM with CSF and white-matter signal, dvars, framewise-displacement and translations and rotations in x-, y- and z-axis as confounds, high-pass filter of 100s and 6mm smoothing. For native-space analyses based on GLM masks, we used individual 1st level z-maps, z > 2.5. For the control analysis based on group level GLM masks, we used FWE-corrected z-maps from the 2nd level analysis. The following contrasts were calculated: CALC-positive = CALC > CTRL or REST, CALC-negative = CALC < CTRL or REST, MEM-positive = MEM > CTRL, MEM-negative = MEM < CTRL.

Artifact and GM masking

To exclude voxels from artifact affected brain areas, we calculated the temporal signal-to-noise ratio (tSNR) from the fMRI BOLD images per subject and voxel in standard 2mm space. We then masked out voxels that were in the lowest 15th percentile in over 66% of participants. These were mainly located in areas with strong susceptibility perturbations, i.e., fronto- and temporo-basal brain areas. Additionally, we masked out the cerebellum and only considered voxels with a gray-matter (GM) probability bigger than 0.5. The final SNR-GM-mask in standard space was applied to the output of the GLM group analysis and to the input matrices for the partial least squares analyses. For the analyses in native space, we additionally used native-space parameter maps to mask CSF-influenced areas (T2 > 90ms), susceptibility-influenced areas (R2' > 9 s^{-1}), voxels with a high percentage of blood volume (CBV >10%, probably driven by larger veins/arteries) and voxels with T2' > 90ms, OEF > 0.9, CBF > 90ml/100g/min.

Partial least squares analysis

Partial least squares (PLS) analyses were performed using the Python pyls library (Python Software Foundation, version 3.8). Mean-centered PLS is a data-reduction method that computes latent variables and corresponding brain patterns, which optimally relate brain signals to the experimental design, contrasting e.g. groups or conditions (McIntosh & Lobaugh, 2004). In our case, the input data matrix contained one row for each subject including all voxels within the SNR-GM-mask in standard 2mm space, and stacked conditions, e.g. CALC and CTRL. In the case of BOLD fMRI data, median values of percent signal change (deviation from either median across CTRL or REST) across 24s (20TRs) per task condition were used, excluding the first 6s per task block to account for the hemodynamic response lag. In the case of mqBOLD data, quantitative OEF, CBF or CMRO2 values per voxel and subject were used for all conditions. With the help of a dummy-coding matrix, the pyls library computes within-condition averages which are column-wise mean-centered (Krishnan et al., 2011). This matrix, $R_{mean\text{-}centered\ (q\ x\ p)}$, which comprises q conditions and p voxels, is then subjected to singular value decomposition, which results in:

$$R'_{mean\text{-}centered} = USV' \qquad [5]$$

where $U_{p \times q}$ are the voxel weights (brain saliences), one row per latent variable (LV) I, that reflect how much this voxel contributes to the effect captured by LV_i. $V_{q \times q}$ are the task saliences (one row per LV) that indicate how each condition contributes to the spatial pattern identified by LV_i. $S_{q \times q}$ are the singular values per LV that reflect the strength of the relationship extracted by each LV_i (McIntosh & Mišić, 2013). The significance of the latent variables, i.e., the entire multivariate pattern, was tested via permutation tests (3000 permutations), the reliability of the brain saliences, i.e., the voxel's contribution to the latent variables, was deduced via bootstrap resampling (3000 samples). Brain regions showing significant effects were identified via the ratio of the brain saliences to the bootstrap standard error (BSR), where a BSR > ±2 is akin to a confidence interval of 95%, if the bootstrap distribution is normal (Krishnan et al., 2011; McIntosh & Mišić, 2013). In this paper, we used PLS analyses to perform group level statistics in order to identify brain regions that differentiate best between a task (CALC or MEM) and a baseline (CTRL or REST) condition. As the same analyses were applied to both BOLD fMRI and mqBOLD data, resulting statistical result maps could be compared across the different parameters. The statistical maps were thresholded with a BSR of ±2 and only clusters with more than 30 voxels were kept for creating group masks. Please note that for correct interpretation, BSR maps must be compared to the design scores (design variables multiplied by brain saliences) of each condition within each LV to know the direction of task differences that is captured within the BSR pattern. In this manuscript, a blue-red BSR pattern indicates a positive task effect, that is voxels with higher values during the task compared to the baseline, whereas blue voxels show the opposite contrast.

BOLD clusters

The BOLD clusters shown in Fig. 2D were based on the PLS analysis of the BOLD data. Resulting statistical maps were thresholded with a BSR > +/-3 using nilearn's region package in python. Connected regions with a minimum region size of 1000 were extracted. Then, upon visual inspection, clusters that apparently were fractionated by the algorithm but that belonged together, visually and based on Yeo's networks (Yeo et al., 2011), were assembled into one.

CBF peak ROIs

In order to compare our data to the CBF data from positron-emission-tomography in the seminal paper from Shulman and colleagues (Shulman, FIEZ, et al., 1997), we calculated median ΔCBF[%] across subjects, with a threshold of CBF < -2%, no correction applied (Fig. S2B). CBF peak ROIs were derived from the PLS-derived statistical group map as shown in Fig. S2B, on the right. We used the atlasreader library in python (Notter et al., 2019) to extract peak coordinates. We then selected the coordinates of nine (out of 15) peaks with the highest positive peak values, plus all seven peaks with negative peak values, to create spheres with 5mm diameter around these coordinates. Within these spheres, median CBF and CMRO2 responses were extracted, comparing CALC versus REST conditions.

Other statistical analyses

For the native space analyses, we calculated median values within each native-space activation ROI (output of the first level GLM, thresholded with z>3.1) per subject and tested significant differences in task compared to baseline via paired-samples t-tests, across subjects. All other statistics were based on median voxel values within a group mask in standard space, by taking the across-subjects median value per voxel in task and in baseline (Fig. 2B, Fig. 3B, Fig. 4A&D). Barplots showing median voxels values were generated via python's seaborn library (Waskom, 2021), with error bars showing 95% confidence interval (CI), using 2000 permutations. If the CI, shown by the error bar, includes zero, the median delta value is not statistically significant.

To test differences in hemodynamics between discordant and concordant voxels, we used paired t-tests on the median subject values, to test for differences in baseline, we used independent sample permutation test on the median voxel values. External, high-resolution maps were downsampled to 2mm MNI standard space before analyses were conducted.

FUNDING

CP has been funded by the Deutsche Forschungsgemeinschaft (DFG, German Research Foundation, ID 395030489), and VR has been funded by the European Research Council (ERC) under the European Union's Horizon 2020 research and innovation program (ERC Starting Grant, ID 759659).

DATA and CODE AVAILABILITY

All raw and processed data from are available in the online repository of OpenNeuro (Epp et al., 2023) (https://openneuro.org/datasets/ds004873). The scripts, python jupyter notebooks, docker container for quantitative parameter map analyses and configuration files for replication of all analyses and figures are available on GitHub (https://github.com/NeuroenergeticsLab/two_modes_of_hemodynamics).

REFERENCES

Addis, D. R., Wong, A. T., & Schacter, D. L. (2007). Remembering the past and imagining the future: Common and distinct neural substrates during event construction and elaboration. *Neuropsychologia*, *45*(7), 1363–1377. https://doi.org/10.1016/j.neuropsychologia.2006.10.016

Alsop, D. C., Detre, J. A., Golay, X., Günther, M., Hendrikse, J., Hernandez-Garcia, L., Lu, H., MacIntosh, B. J., Parkes, L. M., Smits, M., van Osch, M. J. P., Wang, D. J. J., Wong, E. C., & Zaharchuk, G. (2015). Recommended implementation of arterial spin-labeled perfusion MRI for clinical applications: A consensus of the ISMRM perfusion study group and the European consortium for ASL in dementia: Recommended Implementation of ASL for Clinical Applications. *Magnetic Resonance in Medicine*, *73*(1), 102–116. https://doi.org/10.1002/mrm.25197

Amalric, M., & Dehaene, S. (2016). Origins of the brain networks for advanced mathematics in expert mathematicians. *Proceedings of the National Academy of Sciences*, *113*(18), 4909–4917. https://doi.org/10.1073/pnas.1603205113

Ances, B. M., Leontiev, O., Perthen, J. E., Liang, C., Lansing, A. E., & Buxton, R. B. (2008). Regional differences in the coupling of cerebral blood flow and oxygen metabolism changes in response to activation: Implications for BOLD-fMRI. *NeuroImage*, *39*(4), 1510–1521. https://doi.org/10.1016/j.neuroimage.2007.11.015

Andrews-Hanna, J. R., Saxe, R., & Yarkoni, T. (2014). Contributions of episodic retrieval and mentalizing to autobiographical thought: Evidence from functional neuroimaging, resting-state connectivity, and fMRI meta-analyses. *NeuroImage*, *91*, 324–335. https://doi.org/10.1016/j.neuroimage.2014.01.032

Anticevic, A., Cole, M. W., Murray, J. D., Corlett, P. R., Wang, X.-J., & Krystal, J. H. (2012). The role of default network deactivation in cognition and disease. *Trends in Cognitive Sciences*, *16*(12), 584–592. https://doi.org/10.1016/j.tics.2012.10.008

Aoe, J., Watabe, T., Shimosegawa, E., Kato, H., Kanai, Y., Naka, S., Matsunaga, K., Isohashi, K., Tatsumi, M., & Hatazawa, J. (2018). Evaluation of the default-mode network by quantitative 15O-PET: Comparative study between cerebral blood flow and oxygen consumption. *Annals of Nuclear Medicine*, *32*(7), 485–491. https://doi.org/10.1007/s12149-018-1272-x

Attwell, D., Buchan, A. M., Charpak, S., Lauritzen, M., MacVicar, B. A., & Newman, E. A. (2010). Glial and neuronal control of brain blood flow. *Nature*, *468*(7321), 232–243. https://doi.org/10.1038/nature09613

Avants, B., Epstein, C., Grossman, M., & Gee, J. (2008). Symmetric diffeomorphic image registration with cross-correlation: Evaluating automated labeling of elderly and neurodegenerative brain. *Medical Image Analysis*, *12*(1), 26–41. https://doi.org/10.1016/j.media.2007.06.004

Baudrexel, S., Volz, S., Preibisch, C., Klein, J. C., Steinmetz, H., Hilker, R., & Deichmann, R. (2009). Rapid single-scan T2*-mapping using exponential excitation pulses and image-based correction for linear background gradients: T2* Mapping With Field Gradient Correction. *Magnetic Resonance in Medicine*, *62*(1), 263–268. https://doi.org/10.1002/mrm.21971

Bergel, A., Tiran, E., Deffieux, T., Demené, C., Tanter, M., & Cohen, I. (2020). Adaptive modulation of brain hemodynamics across stereotyped running episodes. *Nature Communications*, *11*(1). Scopus. https://doi.org/10.1038/s41467-020-19948-7

Blockley, N. P., Griffeth, V. E. M., & Buxton, R. B. (2012). A general analysis of calibrated BOLD methodology for measuring CMRO2 responses: Comparison of a new approach with existing methods. *NeuroImage*, *60*(1), 279–289. https://doi.org/10.1016/j.neuroimage.2011.11.081

Blockley, N. P., Griffeth, V. E. M., Simon, A. B., & Buxton, R. B. (2013). A review of calibrated blood oxygenation level-dependent (BOLD) methods for the measurement of task-induced changes in brain oxygen metabolism: A REVIEW OF CALIBRATED BOLD METHODS. *NMR in Biomedicine*, *26*(8), 987–1003. https://doi.org/10.1002/nbm.2847

Blockley, N. P., Griffeth, V. E. M., Simon, A. B., Dubowitz, D. J., & Buxton, R. B. (2015). Calibrating the BOLD response without administering gases: Comparison of hypercapnia calibration with calibration using an asymmetric spin echo. *NeuroImage*, *104*, 423–429. https://doi.org/10.1016/j.neuroimage.2014.09.061

Boorman, L., Kennerley, A. J., Johnston, D., Jones, M., Zheng, Y., Redgrave, P., & Berwick, J. (2010). Negative Blood Oxygen Level Dependence in the Rat:A Model for Investigating the Role of Suppression in Neurovascular Coupling. *Journal of Neuroscience*, *30*(12), 4285–4294. https://doi.org/10.1523/JNEUROSCI.6063-09.2010

Boxermann, J.L., Schmainda, K.M., Weisskoff, R.M. (2006). Relative Cerebral Blood Volume Maps Corrected for Contrast Agent Extravasation Significantly Correlate with Glioma Tumor Grade, Whereas Uncorrected Maps Do Not. *Amercian Journal of Neuroradiology*, *27*(4), 859–867.

Boynton, G. M. (2011). Spikes, BOLD, Attention, and Awareness: A comparison of electrophysiological and fMRI signals in V1. *Journal of Vision*, *11*(5), 12. https://doi.org/10.1167/11.5.12

Bright, M. G., Croal, P. L., Blockley, N. P., & Bulte, D. P. (2019). Multiparametric measurement of cerebral physiology using calibrated fMRI. *NeuroImage*, *187*, 128–144. https://doi.org/10.1016/j.neuroimage.2017.12.049

Burianova, H., & Grady, C. L. (2007a). Common and Unique Neural Activations in Autobiographical, Episodic, and Semantic Retrieval. *Journal of Cognitive Neuroscience*, *19*(9), 1520–1534. https://doi.org/10.1162/jocn.2007.19.9.1520

Burianova, H., & Grady, C. L. (2007b). Common and Unique Neural Activations in Autobiographical, Episodic, and Semantic Retrieval. *Journal of Cognitive Neuroscience*, *19*(9), 1520–1534. https://doi.org/10.1162/jocn.2007.19.9.1520

Burianova, H., McIntosh, A. R., & Grady, C. L. (2010). A common functional brain network for autobiographical, episodic, and semantic memory retrieval. *NeuroImage*, *49*(1), 865–874. https://doi.org/10.1016/j.neuroimage.2009.08.066

Buxton, R. B. (2010). Interpreting oxygenation-based neuroimaging signals: The importance and the challenge of understanding brain oxygen metabolism. *Frontiers in Neuroenergetics*. https://doi.org/10.3389/fnene.2010.00008

Buxton, R. B. (2020). The thermodynamics of thinking: Connections between neural activity, energy metabolism and blood flow. *bioRxiv*, 833855. https://doi.org/10.1101/833855

Buxton, R. B. (2023). *Thermodynamic limitations on brain oxygen metabolism: Physiological implications* [Preprint]. Neuroscience. https://doi.org/10.1101/2023.01.06.522942

Buxton, R. B., & Frank, L. R. (1997). A Model for the Coupling between Cerebral Blood Flow and Oxygen Metabolism during Neural Stimulation. *Journal of Cerebral Blood Flow & Metabolism*, *17*(1), 64–72. https://doi.org/10.1097/00004647-199701000-00009

Buxton, R. B., Griffeth, V. E. M., Simon, A. B., & Moradi, F. (2014). Variability of the coupling of blood flow and oxygen metabolism responses in the brain: A problem for interpreting BOLD studies but potentially a new window on the underlying neural activity. *Frontiers in Neuroscience*, *8*. https://doi.org/10.3389/fnins.2014.00139

Cardoso, M. M. B., Sirotin, Y. B., Lima, B., Glushenkova, E., & Das, A. (2012). The neuroimaging signal is a linear sum of neurally distinct stimulus- and task-related components. *Nature Neuroscience*, *15*(9), 1298–1306. https://doi.org/10.1038/nn.3170

Chen, J. J., Uthayakumar, B., & Hyder, F. (2022). Mapping oxidative metabolism in the human brain with calibrated fMRI in health and disease. *Journal of Cerebral Blood Flow & Metabolism*, *42*(7), 1139–1162. https://doi.org/10.1177/0271678X221077338

Cho, J., Kee, Y., Spincemaille, P., Nguyen, T. D., Zhang, J., Gupta, A., Zhang, S., & Wang, Y. (2018). Cerebral metabolic rate of oxygen ($CMRO_2$) mapping by combining quantitative susceptibility mapping (QSM) and quantitative blood oxygenation level-dependent imaging (qBOLD). *Magnetic Resonance in Medicine*, *80*(4), 1595–1604. https://doi.org/10.1002/mrm.27135

Christen, T., Schmiedeskamp, H., Straka, M., Bammer, R., & Zaharchuk, G. (2012). Measuring brain oxygenation in humans using a multiparametric quantitative blood oxygenation level dependent MRI approach. *Magnetic Resonance in Medicine*, *68*(3), 905–911. https://doi.org/10.1002/mrm.23283

Das, A., & Sirotin, Y. B. (2011). What could underlie the trial-related signal? A response to the commentaries by Drs. Kleinschmidt and Muller, and Drs. Handwerker and Bandettini. *NeuroImage*, *55*(4), 1413–1418. https://doi.org/10.1016/j.neuroimage.2010.07.005

Davey, C. G., Pujol, J., & Harrison, B. J. (2016). Mapping the self in the brain's default mode network. *NeuroImage*, *132*, 390–397. https://doi.org/10.1016/j.neuroimage.2016.02.022

Davis, T. L., Kwong, K. K., Weisskoff, R. M., & Rosen, B. R. (1998). Calibrated functional MRI: Mapping the dynamics of oxidative metabolism. *Proceedings of the National Academy of Sciences*, *95*(4), 1834–1839. https://doi.org/10.1073/pnas.95.4.1834

Devonshire, I. M., Papadakis, N. G., Port, M., Berwick, J., Kennerley, A. J., Mayhew, J. E. W., & Overton, P. G. (2012). Neurovascular coupling is brain region-dependent. *NeuroImage*, *59*(3), 1997–2006. https://doi.org/10.1016/j.neuroimage.2011.09.050

Devor, A., Dunn, A. K., Andermann, M. L., Ulbert, I., Boas, D. A., & Dale, A. M. (2003). Coupling of Total Hemoglobin Concentration, Oxygenation, and Neural Activity in Rat Somatosensory Cortex. *Neuron*, *39*(2), 353–359. https://doi.org/10.1016/S0896-6273(03)00403-3

Devor, A., Hillman, E. M. C., Tian, P., Waeber, C., Teng, I. C., Ruvinskaya, L., Shalinsky, M. H., Zhu, H., Haslinger, R. H., Narayanan, S. N., Ulbert, I., Dunn, A. K., Lo, E. H., Rosen, B. R.,

Dale, A. M., Kleinfeld, D., & Boas, D. A. (2008). Stimulus-Induced Changes in Blood Flow and 2-Deoxyglucose Uptake Dissociate in Ipsilateral Somatosensory Cortex. *Journal of Neuroscience*, *28*(53), 14347–14357. https://doi.org/10.1523/JNEUROSCI.4307-08.2008

Devor, A., Tian, P., Nishimura, N., Teng, I. C., Hillman, E. M. C., Narayanan, S. N., Ulbert, I., Boas, D. A., Kleinfeld, D., & Dale, A. M. (2007). Suppressed Neuronal Activity and Concurrent Arteriolar Vasoconstriction May Explain Negative Blood Oxygenation Level-Dependent Signal. *Journal of Neuroscience*, *27*(16), 4452–4459. https://doi.org/10.1523/JNEUROSCI.0134-07.2007

DiNuzzo, M., Dienel, G. A., Behar, K. L., Petroff, O. A., Benveniste, H., Hyder, F., Giove, F., Michaeli, S., Mangia, S., Herculano-Houzel, S., & Rothman, D. L. (2023). Neurovascular coupling is optimized to compensate for the increase in proton production from nonoxidative glycolysis and glycogenolysis during brain activation and maintain homeostasis of pH, $p\,CO_2$, and $p\,O_2$. *Journal of Neurochemistry*, jnc.15839. https://doi.org/10.1111/jnc.15839

Drew, P. J. (2022). Neurovascular coupling: Motive unknown. *Trends in Neurosciences*, S0166223622001618. https://doi.org/10.1016/j.tins.2022.08.004

DuPre, E., Luh, W.-M., & Spreng, R. N. (2016). Multi-echo fMRI replication sample of autobiographical memory, prospection and theory of mind reasoning tasks. *Scientific Data*, *3*(1), 160116. https://doi.org/10.1038/sdata.2016.116

Eichling, J. O., Raichle, M. E., Grubb, R. L., Larson, K. B., & Ter-Pogossian, M. M. (1975). In vivo determination of cerebral blood volume with radioactive oxygen-15 in the monkey. *Circulation Research*, *37*(6), 707–714. https://doi.org/10.1161/01.RES.37.6.707

Ekstrom, A. (2010). How and when the fMRI BOLD signal relates to underlying neural activity: The danger in dissociation. *Brain Research Reviews*, *62*(2), 233–244. https://doi.org/10.1016/j.brainresrev.2009.12.004

Ekstrom, A. D. (2021). Regional variation in neurovascular coupling and why we still lack a Rosetta Stone. *Philosophical Transactions of the Royal Society B: Biological Sciences*, *376*(1815), 20190634. https://doi.org/10.1098/rstb.2019.0634

Esteban, O. (2019). fMRIPrep: A robust preprocessing pipeline for functional MRI. *Nature Methods*, *16*, 14.

Esteban, O., Ciric, R., Finc, K., Blair, R. W., Markiewicz, C. J., Moodie, C. A., Kent, J. D., Goncalves, M., DuPre, E., Gomez, D. E. P., Ye, Z., Salo, T., Valabregue, R., Amlien, I. K., Liem, F., Jacoby, N., Stojić, H., Cieslak, M., Urchs, S., … Gorgolewski, K. J. (2020). Analysis of task-based functional MRI data preprocessed with fMRIPrep. *Nature Protocols*, *15*(7), 2186–2202. https://doi.org/10.1038/s41596-020-0327-3

Fehr, T., Code, C., & Herrmann, M. (2007). Common brain regions underlying different arithmetic operations as revealed by conjunct fMRI–BOLD activation. *Brain Research*, *1172*, 93–102. https://doi.org/10.1016/j.brainres.2007.07.043

Fox, P., & Raichle, M. E. (1986). Focal physiological uncoupling of cerebral blood flow and oxidative metabolism during somatosensory stimulation in human subjects. *Proceedings of the National Academy of Sciences*, *83*(4), 1140–1144. https://doi.org/10.1073/pnas.83.4.1140

Fox, P., Raichle, M., Mintun, M., & Dence, C. (1988). Nonoxidative glucose consumption during focal physiologic neural activity. *Science*, *241*(4864), 462–464. https://doi.org/10.1126/science.3260686

Fracasso, A., Gaglianese, A., Vansteensel, M. J., Aarnoutse, E. J., Ramsey, N. F., Dumoulin, S. O., & Petridou, N. (2022). FMRI and intra-cranial electrocorticography recordings in the same human subjects reveals negative BOLD signal coupled with silenced neuronal activity. *Brain Structure and Function*, *227*(4), 1371–1384. https://doi.org/10.1007/s00429-021-02342-4

Fujita, N., Matsumoto, K., Tanaka, H., Watanabe, Y., & Murase, K. (2006). Quantitative study of changes in oxidative metabolism during visual stimulation using absolute relaxation rates. *NMR in Biomedicine*, *19*(1), 60–68. https://doi.org/10.1002/nbm.1001

Gagnon, L., Sakad i, S., Lesage, F., Musacchia, J. J., Lefebvre, J., Fang, Q., Yucel, M. A., Evans, K. C., Mandeville, E. T., Cohen-Adad, J., Polimeni, J. R., Yaseen, M. A., Lo, E. H., Greve, D. N., Buxton, R. B., Dale, A. M., Devor, A., & Boas, D. A. (2015). Quantifying the Microvascular Origin of BOLD-fMRI from First Principles with Two-Photon Microscopy and an Oxygen-Sensitive Nanoprobe. *Journal of Neuroscience*, *35*(8), 3663–3675. https://doi.org/10.1523/JNEUROSCI.3555-14.2015

Gagnon, L., Sakadžić, S., Lesage, F., Pouliot, P., Dale, A. M., Devor, A., Buxton, R. B., & Boas, D. A. (2016). Validation and optimization of hypercapnic-calibrated fMRI from oxygen-sensitive two-photon microscopy. *Philosophical Transactions of the Royal Society B: Biological Sciences*, *371*(1705), 20150359. https://doi.org/10.1098/rstb.2015.0359

Garcia, D. M., Duhamel, G., & Alsop, D. C. (2005). Efficiency of inversion pulses for background suppressed arterial spin labeling. *Magnetic Resonance in Medicine*, *54*(2), 366–372. https://doi.org/10.1002/mrm.20556

Gauthier, C. J., Desjardins-Crépeau, L., Madjar, C., Bherer, L., & Hoge, R. D. (2012). Absolute quantification of resting oxygen metabolism and metabolic reactivity during functional activation using QUO2 MRI. *NeuroImage*, *63*(3), 1353–1363. https://doi.org/10.1016/j.neuroimage.2012.07.065

Gauthier, C. J., & Hoge, R. D. (2012). Magnetic resonance imaging of resting OEF and CMRO2 using a generalized calibration model for hypercapnia and hyperoxia. *NeuroImage*, *60*(2), 1212–1225. https://doi.org/10.1016/j.neuroimage.2011.12.056

Germuska, M., & Wise, R. G. (2019). Calibrated fMRI for mapping absolute CMRO2: Practicalities and prospects. *NeuroImage*, *187*, 145–153. https://doi.org/10.1016/j.neuroimage.2018.03.068

Glasser, M. F. (2016). *A multi-modal parcellation of human cerebral cortex*. 11. https://doi.org/10.1038/nature18933

Gorgolewski, K., Burns, C. D., Madison, C., Clark, D., Halchenko, Y. O., Waskom, M. L., & Ghosh, S. S. (2011). Nipype: A Flexible, Lightweight and Extensible Neuroimaging Data Processing Framework in Python. *Frontiers in Neuroinformatics*, *5*. https://doi.org/10.3389/fninf.2011.00013

Göttler, J., Kaczmarz, S., Kallmayer, M., Wustrow, I., Eckstein, H.-H., Zimmer, C., Sorg, C., Preibisch, C., & Hyder, F. (2019). Flow-metabolism uncoupling in patients with asymptomatic unilateral carotid artery stenosis assessed by multi-modal magnetic

resonance imaging. *Journal of Cerebral Blood Flow & Metabolism*, *39*(11), 2132–2143. https://doi.org/10.1177/0271678X18783369

Griffeth, V. E. M., & Buxton, R. B. (2011). A theoretical framework for estimating cerebral oxygen metabolism changes using the calibrated-BOLD method: Modeling the effects of blood volume distribution, hematocrit, oxygen extraction fraction, and tissue signal properties on the BOLD signal. *NeuroImage*, *58*(1), 198–212. https://doi.org/10.1016/j.neuroimage.2011.05.077

Grubb, R. L., Raichle, M. E., Eichling, J. O., & Ter-Pogossian, M. M. (1974). The Effects of Changes in Pa CO_2 Cerebral Blood Volume, Blood Flow, and Vascular Mean Transit Time. *Stroke*, *5*(5), 630–639. https://doi.org/10.1161/01.STR.5.5.630

Hall, C. N., Howarth, C., Kurth-Nelson, Z., & Mishra, A. (2016). Interpreting BOLD: Towards a dialogue between cognitive and cellular neuroscience. *Philosophical Transactions of the Royal Society B: Biological Sciences*, *371*(1705), 20150348. https://doi.org/10.1098/rstb.2015.0348

He, X., & Yablonskiy, D. A. (2007). Quantitative BOLD: Mapping of human cerebral deoxygenated blood volume and oxygen extraction fraction: Default state. *Magnetic Resonance in Medicine*, *57*(1), 115–126. https://doi.org/10.1002/mrm.21108

Hedderich, D., Kluge, A., Pyka, T., Zimmer, C., Kirschke, J. S., Wiestler, B., & Preibisch, C. (2019). Consistency of normalized cerebral blood volume values in glioblastoma using different leakage correction algorithms on dynamic susceptibility contrast magnetic resonance imaging data without and with preload. *Journal of Neuroradiology*, *46*(1), 44–51. https://doi.org/10.1016/j.neurad.2018.04.006

Heeger, D. J., Huk, A. C., Geisler, W. S., & Albrecht, D. G. (2000). Spikes versus BOLD: What does neuroimaging tell us about neuronal activity? *Nature Neuroscience*, *3*(7), Article 7. https://doi.org/10.1038/76572

Hillman, E. M. C. (2014). Coupling Mechanism and Significance of the BOLD Signal: A Status Report. *Annual Review of Neuroscience*, *37*(1), 161–181. https://doi.org/10.1146/annurev-neuro-071013-014111

Hirsch, N. M., & Preibisch, C. (2013). T2* Mapping with Background Gradient Correction Using Different Excitation Pulse Shapes. *American Journal of Neuroradiology*, *34*(6), E65–E68. https://doi.org/10.3174/ajnr.A3021

Hirsch, N. M., Toth, V., Förschler, A., Kooijman, H., Zimmer, C., & Preibisch, C. (2014). Technical considerations on the validity of blood oxygenation level-dependent-based MR assessment of vascular deoxygenation: BOLD-BASED ASSESSMENT OF VASCULAR DEOXYGENATION. *NMR in Biomedicine*, *27*(7), 853–862. https://doi.org/10.1002/nbm.3131

Howarth, C., Mishra, A., & Hall, C. N. (2021). More than just summed neuronal activity: How multiple cell types shape the BOLD response. *Philosophical Transactions of the Royal Society B: Biological Sciences*, *376*(1815), 20190630. https://doi.org/10.1098/rstb.2019.0630

Huck, J., Wanner, Y., Fan, A. P., Jäger, A.-T., Grahl, S., Schneider, U., Villringer, A., Steele, C. J., Tardif, C. L., Bazin, P.-L., & Gauthier, C. J. (2019). High resolution atlas of the venous brain vasculature from 7 T quantitative susceptibility maps. *Brain Structure and Function*, *224*(7), 2467–2485. https://doi.org/10.1007/s00429-019-01919-4

Huo, B.-X., Smith, J. B., & Drew, P. J. (2014). Neurovascular coupling and decoupling in the cortex during voluntary locomotion. *The Journal of Neuroscience: The Official Journal of the Society for Neuroscience*, *34*(33), 10975–10981. https://doi.org/10.1523/JNEUROSCI.1369-14.2014

Hyder, D. S. F. (2010). Neurovascular and neurometabolic couplings in dynamic calibrated fMRI: Transient oxidative neuroenergetics for block-design and event-related paradigms. *Frontiers in Neuroenergetics*. https://doi.org/10.3389/fnene.2010.00018

Hyder, D. S. F., Sanganahalli, B., Herman, P., Coman, D., Maandag, N., Behar, K., Blumenfeld, H., & Rothman, D. (2010). Neurovascular and Neurometabolic Couplings in Dynamic Calibrated fMRI: Transient Oxidative Neuroenergetics for Block-Design and Event-Related Paradigms. *Frontiers in Neuroenergetics*, *2*. https://www.frontiersin.org/articles/10.3389/fnene.2010.00018

Ino, T., Nakai, R., Azuma, T., Kimura, T., & Fukuyama, H. (2011). Brain Activation During Autobiographical Memory Retrieval with Special Reference to Default Mode Network. *The Open Neuroimaging Journal*, *5*, 14–23. https://doi.org/10.2174/1874440001105010014

Ito, H., Kubo, H., Takahashi, K., Nishijima, K.-I., Ukon, N., Nemoto, A., Sugawara, S., Yamakuni, R., Ibaraki, M., & Ishii, S. (2021). Integrated PET/MRI scanner with oxygen-15 labeled gases for quantification of cerebral blood flow, cerebral blood volume, cerebral oxygen extraction fraction and cerebral metabolic rate of oxygen. *Annals of Nuclear Medicine*, *35*(4), 421–428. https://doi.org/10.1007/s12149-021-01578-8

Jenkinson, M., Beckmann, C. F., Behrens, T. E. J., Woolrich, M. W., & Smith, S. M. (2012). FSL. *NeuroImage*, *62*(2), 782–790. https://doi.org/10.1016/j.neuroimage.2011.09.015

Kaczmarz, S., Göttler, J., Zimmer, C., Hyder, F., & Preibisch, C. (2020). Characterizing white matter fiber orientation effects on multi-parametric quantitative BOLD assessment of oxygen extraction fraction. *Journal of Cerebral Blood Flow & Metabolism*, *40*(4), 760–774. https://doi.org/10.1177/0271678X19839502

Kaczmarz, S., Hyder, F., & Preibisch, C. (2020). Oxygen extraction fraction mapping with multi-parametric quantitative BOLD MRI: Reduced transverse relaxation bias using 3D-GraSE imaging. *NeuroImage*, *220*, 117095. https://doi.org/10.1016/j.neuroimage.2020.117095

Kim, S.-G., & Ogawa, S. (2012). Biophysical and Physiological Origins of Blood Oxygenation Level-Dependent fMRI Signals. *Journal of Cerebral Blood Flow & Metabolism*, *32*(7), 1188–1206. https://doi.org/10.1038/jcbfm.2012.23

Kluge, A., Lukas, M., Toth, V., Pyka, T., Zimmer, C., & Preibisch, C. (2016). Analysis of three leakage-correction methods for DSC-based measurement of relative cerebral blood volume with respect to heterogeneity in human gliomas. *Magnetic Resonance Imaging*, *34*(4), 410–421. https://doi.org/10.1016/j.mri.2015.12.015

Koush, Y., de Graaf, R. A., Kupers, R., Dricot, L., Ptito, M., Behar, K. L., Rothman, D. L., & Hyder, F. (2021). Metabolic underpinnings of activated and deactivated cortical areas in human brain. *Journal of Cerebral Blood Flow & Metabolism*, *41*(5), 986–1000. https://doi.org/10.1177/0271678X21989186

Krishnan, A., Williams, L. J., McIntosh, A. R., & Abdi, H. (2011). Partial Least Squares (PLS) methods for neuroimaging: A tutorial and review. *NeuroImage*, *56*(2), 455–475. https://doi.org/10.1016/j.neuroimage.2010.07.034

Kufer, J., Preibisch, C., Epp, S., Göttler, J., Schmitzer, L., Zimmer, C., Hyder, F., & Kaczmarz, S. (2022). Imaging effective oxygen diffusivity in the human brain with multiparametric magnetic resonance imaging. *Journal of Cerebral Blood Flow & Metabolism*, *42*(2), 349–363. https://doi.org/10.1177/0271678X211048412

Lee, H., & Wehrli, F. W. (2022). Whole-brain 3D mapping of oxygen metabolism using constrained quantitative BOLD. *NeuroImage*, *250*, 118952. https://doi.org/10.1016/j.neuroimage.2022.118952

Leenders, K. L., Perani, D., Lammertsma, A. A., Heather, J. D., Buckingham, P., Jones, T., Healy, M. J. R., Gibbs, J. M., Wise, R. J. S., Hatazawa, J., Herold, S., Beaney, R. P., Brooks, D. J., Spinks, T., Rhodes, C., & Frackowiak, R. S. J. (1990). CEREBRAL BLOOD FLOW, BLOOD VOLUME AND OXYGEN UTILIZATION: NORMAL VALUES AND EFFECT OF AGE. *Brain*, *113*(1), 27–47. https://doi.org/10.1093/brain/113.1.27

Leithner, C., & Royl, G. (2014). The Oxygen Paradox of Neurovascular Coupling. *Journal of Cerebral Blood Flow & Metabolism*, *34*(1), 19–29. https://doi.org/10.1038/jcbfm.2013.181

Leithner, C., Royl, G., Offenhauser, N., Füchtemeier, M., Kohl-Bareis, M., Villringer, A., Dirnagl, U., & Lindauer, U. (2010). Pharmacological Uncoupling of Activation Induced Increases in CBF and CMRO $_2$. *Journal of Cerebral Blood Flow & Metabolism*, *30*(2), 311–322. https://doi.org/10.1038/jcbfm.2009.211

Leontiev, O., & Buxton, R. B. (2007). Reproducibility of BOLD, perfusion, and CMRO2 measurements with calibrated-BOLD fMRI. *NeuroImage*, *35*(1), 175–184. https://doi.org/10.1016/j.neuroimage.2006.10.044

Liang, X., Zou, Q., He, Y., & Yang, Y. (2013). Coupling of functional connectivity and regional cerebral blood flow reveals a physiological basis for network hubs of the human brain. *Proceedings of the National Academy of Sciences*, *110*(5), 1929–1934. https://doi.org/10.1073/pnas.1214900110

Lin, P., Hasson, U., Jovicich, J., & Robinson, S. (2011a). A Neuronal Basis for Task-Negative Responses in the Human Brain. *Cerebral Cortex*, *21*(4), 821–830. https://doi.org/10.1093/cercor/bhq151

Lin, P., Hasson, U., Jovicich, J., & Robinson, S. (2011b). A Neuronal Basis for Task-Negative Responses in the Human Brain. *Cerebral Cortex*, *21*(4), 821–830. https://doi.org/10.1093/cercor/bhq151

Liu, E. Y., Guo, J., Simon, A. B., Haist, F., Dubowitz, D. J., & Buxton, R. B. (2020). The potential for gas-free measurements of absolute oxygen metabolism during both baseline and activation states in the human brain. *NeuroImage*, *207*, 116342. https://doi.org/10.1016/j.neuroimage.2019.116342

Logothetis, N. K., Pauls, J., Augath, M., Trinath, T., & Oeltermann, A. (2001). *Neurophysiological investigation of the basis of the fMRI signal*. *412*.

Lüsebrink, F., Mattern, H., Yakupov, R., Acosta-Cabronero, J., Ashtarayeh, M., Oeltze-Jafra, S., & Speck, O. (2021). Comprehensive ultrahigh resolution whole brain in vivo MRI

dataset as a human phantom. *Scientific Data*, *8*(1), 138. https://doi.org/10.1038/s41597-021-00923-w

Ma, Y., Sun, H., Cho, J., Mazerolle, E. L., Wang, Y., & Pike, G. B. (2020). Cerebral OEF quantification: A comparison study between quantitative susceptibility mapping and dual-gas calibrated BOLD imaging. *Magnetic Resonance in Medicine*, *83*(1), 68–82. https://doi.org/10.1002/mrm.27907

McIntosh, A. R., & Lobaugh, N. J. (2004). Partial least squares analysis of neuroimaging data: Applications and advances. *NeuroImage*, *23*, S250–S263. https://doi.org/10.1016/j.neuroimage.2004.07.020

McIntosh, A. R., & Mišić, B. (2013). Multivariate Statistical Analyses for Neuroimaging Data. *Annual Review of Psychology*, *64*(1), 499–525. https://doi.org/10.1146/annurev-psych-113011-143804

Mullinger, K. J., Mayhew, S. D., Bagshaw, A. P., Bowtell, R., & Francis, S. T. (2014). Evidence that the negative BOLD response is neuronal in origin: A simultaneous EEG–BOLD–CBF study in humans. *NeuroImage*, *94*, 263–274. https://doi.org/10.1016/j.neuroimage.2014.02.029

Mutsaerts, H. J. M. M., Steketee, R. M. E., Heijtel, D. F. R., Kuijer, J. P. A., van Osch, M. J. P., Majoie, C. B. L. M., Smits, M., & Nederveen, A. J. (2014). Inter-Vendor Reproducibility of Pseudo-Continuous Arterial Spin Labeling at 3 Tesla. *PLoS ONE*, *9*(8), e104108. https://doi.org/10.1371/journal.pone.0104108

Nagaoka, T., Zhao, F., Wang, P., Harel, N., Kennan, R. P., Ogawa, S., & Kim, S.-G. (2006). Increases in Oxygen Consumption without Cerebral Blood Volume Change during Visual Stimulation under Hypotension Condition. *Journal of Cerebral Blood Flow & Metabolism*, *26*(8), 1043–1051. https://doi.org/10.1038/sj.jcbfm.9600251

Nöth, U., Volz, S., Hattingen, E., & Deichmann, R. (2014). An improved method for retrospective motion correction in quantitative T2* mapping. *NeuroImage*, *92*, 106–119. https://doi.org/10.1016/j.neuroimage.2014.01.050

Notter, M., Gale, D., Herholz, P., Markello, R., Notter-Bielser, M.-L., & Whitaker, K. (2019). AtlasReader: A Python package to generate coordinate tables, region labels, and informative figures from statistical MRI images. *Journal of Open Source Software*, *4*(34), 1257. https://doi.org/10.21105/joss.01257

Pasley, B. N., Inglis, B. A., & Freeman, R. D. (2007). Analysis of oxygen metabolism implies a neural origin for the negative BOLD response in human visual cortex. *NeuroImage*, *36*(2), 269–276. https://doi.org/10.1016/j.neuroimage.2006.09.015

Pfefferbaum, A., Chanraud, S., Pitel, A.-L., Muller-Oehring, E., Shankaranarayanan, A., Alsop, D. C., Rohlfing, T., & Sullivan, E. V. (2011). Cerebral Blood Flow in Posterior Cortical Nodes of the Default Mode Network Decreases with Task Engagement but Remains Higher than in Most Brain Regions. *Cerebral Cortex*, *21*(1), 233–244. https://doi.org/10.1093/cercor/bhq090

Phillips, A. A., Chan, F. H., Zheng, M. M. Z., Krassioukov, A. V., & Ainslie, P. N. (2016). Neurovascular coupling in humans: Physiology, methodological advances and clinical implications. *Journal of Cerebral Blood Flow & Metabolism*, *36*(4), 647–664. https://doi.org/10.1177/0271678X15617954

Pike, G. B. (2012). Quantitative functional MRI: Concepts, issues and future challenges. *NeuroImage*, *62*(2), 1234–1240. https://doi.org/10.1016/j.neuroimage.2011.10.046

Preibisch, C., Volz, S., Anti, S., & Deichmann, R. (2008). Exponential excitation pulses for improved water content mapping in the presence of background gradients. *Magnetic Resonance in Medicine*, *60*(4), 908–916. https://doi.org/10.1002/mrm.21730

Raichle, M. E., MacLeod, A. M., Snyder, A. Z., Powers, W. J., Gusnard, D. A., & Shulman, G. L. (2001). A default mode of brain function. *Proceedings of the National Academy of Sciences*, *98*(2), 676–682. https://doi.org/10.1073/pnas.98.2.676

Rees, G., Friston, K., & Koch, C. (2000). A direct quantitative relationship between the functional properties of human and macaque V5. *Nature Neuroscience*, *3*(7), 716–723. https://doi.org/10.1038/76673

Restom, K., Perthen, J. E., & Liu, T. T. (2008). Calibrated fMRI in the medial temporal lobe during a memory-encoding task. *NeuroImage*, *40*(4), 1495–1502. https://doi.org/10.1016/j.neuroimage.2008.01.038

Rossetti, G. M., d'Avossa, G., Rogan, M., Macdonald, J. H., Oliver, S. J., & Mullins, P. G. (2021). Reversal of neurovascular coupling in the default mode network: Evidence from hypoxia. *Journal of Cerebral Blood Flow & Metabolism*, *41*(4), 805–818. https://doi.org/10.1177/0271678X20930827

Roy, R. K., Althammer, F., Seymour, A. J., Du, W., Biancardi, V. C., Hamm, J. P., Filosa, J. A., Brown, C. H., & Stern, J. E. (2021). Inverse neurovascular coupling contributes to positive feedback excitation of vasopressin neurons during a systemic homeostatic challenge. *Cell Reports*, *37*(5), 109925. https://doi.org/10.1016/j.celrep.2021.109925

Sanganahalli, B. G., Herman, P., Rothman, D. L., Blumenfeld, H., & Hyder, F. (2016). Metabolic demands of neural-hemodynamic associated and disassociated areas in brain. *Journal of Cerebral Blood Flow & Metabolism*, *36*(10), 0271678X16664531. https://doi.org/10.1177/0271678X16664531

Schridde, U., Khubchandani, M., Motelow, J. E., Sanganahalli, B. G., Hyder, F., & Blumenfeld, H. (2008). Negative BOLD with Large Increases in Neuronal Activity. *Cerebral Cortex*, *18*(8), 1814–1827. https://doi.org/10.1093/cercor/bhm208

Shaw, K., Bell, L., Boyd, K., Grijseels, D. M., Clarke, D., Bonnar, O., Crombag, H. S., & Hall, C. N. (2021a). Neurovascular coupling and oxygenation are decreased in hippocampus compared to neocortex because of microvascular differences. *Nature Communications*, *12*(1), 3190. https://doi.org/10.1038/s41467-021-23508-y

Shaw, K., Bell, L., Boyd, K., Grijseels, D. M., Clarke, D., Bonnar, O., Crombag, H. S., & Hall, C. N. (2021b). Neurovascular coupling and oxygenation are decreased in hippocampus compared to neocortex because of microvascular differences. *Nature Communications*, *12*(1), 3190. https://doi.org/10.1038/s41467-021-23508-y

Shih, Y.-Y. I., Wey, H.-Y., De La Garza, B. H., & Duong, T. Q. (2011a). Striatal and Cortical BOLD, Blood Flow, Blood Volume, Oxygen Consumption, and Glucose Consumption Changes in Noxious Forepaw Electrical Stimulation. *Journal of Cerebral Blood Flow & Metabolism*, *31*(3), 832–841. https://doi.org/10.1038/jcbfm.2010.173

Shih, Y.-Y. I., Wey, H.-Y., De La Garza, B. H., & Duong, T. Q. (2011b). Striatal and Cortical BOLD, Blood Flow, Blood Volume, Oxygen Consumption, and Glucose Consumption Changes

in Noxious Forepaw Electrical Stimulation. *Journal of Cerebral Blood Flow & Metabolism*, *31*(3), 832–841. https://doi.org/10.1038/jcbfm.2010.173

Shmuel, A., Augath, M., Oeltermann, A., & Logothetis, N. K. (2006). Negative functional MRI response correlates with decreases in neuronal activity in monkey visual area V1. *Nature Neuroscience*, *9*(4), 569–577. https://doi.org/10.1038/nn1675

Shmuel, A., Yacoub, E., Pfeuffer, J., Van de Moortele, P.-F., Adriany, G., Hu, X., & Ugurbil, K. (2002). Sustained Negative BOLD, Blood Flow and Oxygen Consumption Response and Its Coupling to the Positive Response in the Human Brain. *Neuron*, *36*(6), 1195–1210. https://doi.org/10.1016/S0896-6273(02)01061-9

Shulman, G. L., Corbetta, M., Buckner, R. L., Fiez, J. A., Miezin, F. M., Raichle, M. E., & Petersen, S. E. (1997). Common Blood Flow Changes across Visual Tasks: I. Increases in Subcortical Structures and Cerebellum but Not in Nonvisual Cortex. *Journal of Cognitive Neuroscience*, *9*(5), 624–647. https://doi.org/10.1162/jocn.1997.9.5.624

Shulman, G. L., FIEZ, J. A., Corbetta, M., Buckner, R. L., Miezin, F. M., Raichle, M. E., & Petersen, S. E. (1997). Common Blood Flow Changes across Visual Tasks: II. Decreases in Cerebral Cortex. *Journal of cognitive neuroscience*, *9*(5), 648–663. https://doi.org/10.1162/jocn.1997.9.5.648

Siero, J. C., Hermes, D., Hoogduin, H., Luijten, P. R., Petridou, N., & Ramsey, N. F. (2013). BOLD Consistently Matches Electrophysiology in Human Sensorimotor Cortex at Increasing Movement Rates: A Combined 7T fMRI and ECoG Study on Neurovascular Coupling. *Journal of Cerebral Blood Flow & Metabolism*, *33*(9), 1448–1456. https://doi.org/10.1038/jcbfm.2013.97

Singh, K. D., & Fawcett, I. P. (2008). Transient and linearly graded deactivation of the human default-mode network by a visual detection task. *NeuroImage*, *41*(1), 100–112. https://doi.org/10.1016/j.neuroimage.2008.01.051

Sirotin, Y. B., & Das, A. (2009). Anticipatory haemodynamic signals in sensory cortex not predicted by local neuronal activity. *Nature*, *457*(7228), 475–479. https://doi.org/10.1038/nature07664

Smallwood, J., Bernhardt, B. C., Leech, R., Bzdok, D., Jefferies, E., & Margulies, D. S. (2021). The default mode network in cognition: A topographical perspective. *Nature Reviews Neuroscience*, *22*(8), 503–513. https://doi.org/10.1038/s41583-021-00474-4

Smith, S. M., Jenkinson, M., Woolrich, M. W., Beckmann, C. F., Behrens, T. E. J., Johansen-Berg, H., Bannister, P. R., De Luca, M., Drobnjak, I., Flitney, D. E., Niazy, R. K., Saunders, J., Vickers, J., Zhang, Y., De Stefano, N., Brady, J. M., & Matthews, P. M. (2004). Advances in functional and structural MR image analysis and implementation as FSL. *NeuroImage*, *23*, S208–S219. https://doi.org/10.1016/j.neuroimage.2004.07.051

Spreng, R. N., & Grady, C. L. (2010). Patterns of Brain Activity Supporting Autobiographical Memory, Prospection, and Theory of Mind, and Their Relationship to the Default Mode Network. *Journal of Cognitive Neuroscience*, *22*(6), 1112–1123. https://doi.org/10.1162/jocn.2009.21282

Spreng, R. N., Stevens, W. D., Chamberlain, J. P., Gilmore, A. W., & Schacter, D. L. (2010). Default network activity, coupled with the frontoparietal control network, supports goal-directed cognition. *NeuroImage*, *53*(1), 303–317. https://doi.org/10.1016/j.neuroimage.2010.06.016

Stefanovic, B., Warnking, J. M., & Pike, G. B. (2004). Hemodynamic and metabolic responses to neuronal inhibition. *NeuroImage*, *22*(2), 771–778. https://doi.org/10.1016/j.neuroimage.2004.01.036

Stiernman, L. J., Grill, F., Hahn, A., Rischka, L., Lanzenberger, R., Panes Lundmark, V., Riklund, K., Axelsson, J., & Rieckmann, A. (2021). Dissociations between glucose metabolism and blood oxygenation in the human default mode network revealed by simultaneous PET-fMRI. *Proceedings of the National Academy of Sciences*, *118*(27), e2021913118. https://doi.org/10.1073/pnas.2021913118

Stone, A. J., & Blockley, N. P. (2017). A streamlined acquisition for mapping baseline brain oxygenation using quantitative BOLD. *NeuroImage*, *147*, 79–88. https://doi.org/10.1016/j.neuroimage.2016.11.057

Takata, N., Sugiura, Y., Yoshida, K., Koizumi, M., Hiroshi, N., Honda, K., Yano, R., Komaki, Y., Matsui, K., Suematsu, M., Mimura, M., Okano, H., & Tanaka, K. F. (2018). Optogenetic astrocyte activation evokes BOLD fMRI response with oxygen consumption without neuronal activity modulation. *Glia*, *66*(9), 2013–2023. https://doi.org/10.1002/glia.23454

Tsvetanov, K. A., Henson, R. N. A., & Rowe, J. B. (2020). Separating vascular and neuronal effects of age on fMRI BOLD signals. *Philosophical Transactions of the Royal Society B: Biological Sciences*, *376*(1815), 20190631. https://doi.org/10.1098/rstb.2019.0631

Uhlirova, H., Kılıç, K., Tian, P., Thunemann, M., Desjardins, M., Saisan, P. A., Sakadžić, S., Ness, T. V., Mateo, C., Cheng, Q., Weldy, K. L., Razoux, F., Vandenberghe, M., Cremonesi, J. A., Ferri, C. G., Nizar, K., Sridhar, V. B., Steed, T. C., Abashin, M., … Devor, A. (2016). Cell type specificity of neurovascular coupling in cerebral cortex. *eLife*, *5*, e14315. https://doi.org/10.7554/eLife.14315

Uludağ, K., Dubowitz, D. J., Yoder, E. J., Restom, K., Liu, T. T., & Buxton, R. B. (2004). Coupling of cerebral blood flow and oxygen consumption during physiological activation and deactivation measured with fMRI. *NeuroImage*, *23*(1), 148–155. https://doi.org/10.1016/j.neuroimage.2004.05.013

Vanzetta, I., & Grinvald, A. (1999). Increased Cortical Oxidative Metabolism Due to Sensory Stimulation: Implications for Functional Brain Imaging. *Science*, *286*(5444), 1555–1558. https://doi.org/10.1126/science.286.5444.1555

Waskom, M. (2021). seaborn: Statistical data visualization. *Journal of Open Source Software*, *6*(60), 3021. https://doi.org/10.21105/joss.03021

Wilson, R., Mullinger, K. J., Francis, S. T., & Mayhew, S. D. (2019). The relationship between negative BOLD responses and ERS and ERD of alpha/beta oscillations in visual and motor cortex. *NeuroImage*, *199*, 635–650. https://doi.org/10.1016/j.neuroimage.2019.06.009

Wise, R. G., Harris, A. D., Stone, A. J., & Murphy, K. (2013). Measurement of OEF and absolute CMRO2: MRI-based methods using interleaved and combined hypercapnia and hyperoxia. *NeuroImage*, *83*, 135–147. https://doi.org/10.1016/j.neuroimage.2013.06.008

Yablonskiy, D. A., & Haacke, E. M. (1994). Theory of NMR signal behavior in magnetically inhomogeneous tissues: The static dephasing regime. *Magnetic Resonance in Medicine*, *32*(6), 749–763. https://doi.org/10.1002/mrm.1910320610

Yeo, B. T., Krienen, F. M., Sepulcre, J., Sabuncu, M. R., Lashkari, D., Hollinshead, M., Roffman, J. L., Smoller, J. W., Zöllei, L., Polimeni, J. R., Fischl, B., Liu, H., & Buckner, R. L. (2011). The organization of the human cerebral cortex estimated by intrinsic functional connectivity. *Journal of Neurophysiology*, *106*(3), 1125–1165. https://doi.org/10.1152/jn.00338.2011

Zaldivar, D., Rauch, A., Whittingstall, K., Logothetis, N. K., & Goense, J. (2014). Dopamine-Induced Dissociation of BOLD and Neural Activity in Macaque Visual Cortex. *Current Biology*, *24*(23), 2805–2811. https://doi.org/10.1016/j.cub.2014.10.006

Zhang, J., Liu, T., Gupta, A., Spincemaille, P., Nguyen, T. D., & Wang, Y. (2015). Quantitative mapping of cerebral metabolic rate of oxygen ($CMRO_2$) using quantitative susceptibility mapping (QSM): Quantitative $CMRO_2$ Mapping Using QSM. *Magnetic Resonance in Medicine*, *74*(4), 945–952. https://doi.org/10.1002/mrm.25463

Zhang, Q., Roche, M., Gheres, K. W., Chaigneau, E., Kedarasetti, R. T., Haselden, W. D., Charpak, S., & Drew, P. J. (2019). Cerebral oxygenation during locomotion is modulated by respiration. *Nature Communications*, *10*(1). Scopus. https://doi.org/10.1038/s41467-019-13523-5

Zhang, Y., Du, W., Yin, Y., Li, H., Liu, Z., Yang, Y., Han, Y., & Gao, J.-H. (2021). Impaired cerebral vascular and metabolic responses to parametric N-back tasks in subjective cognitive decline. *Journal of Cerebral Blood Flow & Metabolism*, *41*(10), 2743–2755. https://doi.org/10.1177/0271678X211012153